

# Journal of Materials Chemistry A

Materials for energy and sustainability

Accepted Manuscript

This article can be cited before page numbers have been issued, to do this please use: M. A. Rodriguez-Olguin, R. Lipin, E. Castañeda-Morales, C. Flox Donoso, T. Kallio, M. Vandichel, A. Susarrey-Arce, M. Suominen, F. Ruiz-Zepeda, A. Manzo-Robledo and H. J.G.E. Gardeniers, *J. Mater. Chem. A*, 2024, DOI: 10.1039/D4TA04116J.



This is an Accepted Manuscript, which has been through the Royal Society of Chemistry peer review process and has been accepted for publication.

Accepted Manuscripts are published online shortly after acceptance, before technical editing, formatting and proof reading. Using this free service, authors can make their results available to the community, in citable form, before we publish the edited article. We will replace this Accepted Manuscript with the edited and formatted Advance Article as soon as it is available.

You can find more information about Accepted Manuscripts in the [Information for Authors](#).

Please note that technical editing may introduce minor changes to the text and/or graphics, which may alter content. The journal's standard [Terms & Conditions](#) and the [Ethical guidelines](#) still apply. In no event shall the Royal Society of Chemistry be held responsible for any errors or omissions in this Accepted Manuscript or any consequences arising from the use of any information it contains.

# Temperature Promotes Selectivity During Electrochemical View Article Online DOI: 10.1039/C4TA04116J

## CO<sub>2</sub> Reduction on NiO:SnO<sub>2</sub> Nanofibers

M. A. Rodriguez-Olguin,<sup>1,#</sup> R. Lipin,<sup>2,#</sup> M. Suominen,<sup>3</sup> F. Ruiz-Zepeda,<sup>4,5</sup> E. Castañeda-Morales,<sup>6</sup> A. Manzo-Robledo,<sup>6</sup> J.G.E. Gardeniers,<sup>1</sup> C. Flox,<sup>3,7,\*</sup> T. Kallio,<sup>3,\*</sup> M. Vandichel,<sup>2,\*</sup> A. Susarrey-Arce<sup>1,\*</sup>

<sup>1</sup>Mesoscale Chemical Systems, MESA+ Institute, University of Twente, P.O. Box 217, Enschede7500AE, The Netherlands

<sup>2</sup>School of Chemical Sciences and Chemical Engineering, Bernal Institute, University of Limerick, Limerick V94 T9PX, Republic of Ireland

<sup>3</sup>Department of Chemistry and Materials Science, Aalto University School of Chemical Engineering, Kemistintie 1, 02015 Espoo, Finland

<sup>4</sup>Department of Materials Chemistry, National Institute of Chemistry, Hajdrihova 19, 1000, Ljubljana, Slovenia

<sup>5</sup>Department of Physics and Chemistry of Materials, Institute of Metals and Technology, Lepi pot 11, Ljubljana, Slovenia

<sup>6</sup>Instituto Politécnico Nacional, Laboratorio de Electroquímica y Corrosión. Escuela Superior de Ingeniería Química e Industrias Extractivas, Av. Instituto Politécnico Nacional S/N, Unidad Profesional Adolfo López Mateos, CP 07708 CDMX, Mexico

<sup>7</sup>Department of Electrical Energy Storage, Iberian Centre for Research in Energy Storage, Avda. de las Letras, s/n, Campus University of Extremadura, 10004 Cáceres

#These authors contributed equally to this work

\*Corresponding author(s): cristina.flox@ciiae.org; tanja.kallio@aalto.fi; matthias.vandichel@ul.ie; a.susarreyarce@utwente.nl

**Keywords:** Temperature, Selectivity, CO<sub>2</sub> Electroreduction, Formate, NiO, SnO<sub>2</sub>, Nanofibers



## Highlights

View Article Online  
DOI: 10.1039/D4TA04116J

1. NiO:SnO<sub>2</sub> nanofibers, composed of well-packed NiO and SnO<sub>2</sub> nanocrystals, promote CO<sub>2</sub> electroreduction.
2. Contrary to the expected parasitic hydrogen evolution reaction, NiO:SnO<sub>2</sub> nanofibers exhibit higher CO<sub>2</sub> selectivity to formate above room temperatures.
3. Chemical, morphological, structural characterization, *in-situ* DEMS, and computational methods enable the understanding of CO<sub>2</sub> electroreduction reaction mechanisms.



**Abstract**View Article Online  
DOI: 10.1039/D4TA04116J

Electrolyzers operate over a range of temperatures; hence, it is crucial to design electrocatalysts that do not compromise the product distribution unless temperature can promote selectivity. This work reports a synthetic approach based on electrospinning to produce NiO:SnO<sub>2</sub> nanofibers (NFs) for selectively reducing CO<sub>2</sub> to formate above room temperature. The NFs comprise compact, but disjoined NiO and SnO<sub>2</sub> nanocrystals identified with STEM. The results are attributed to the segregation of NiO and SnO<sub>2</sub> confirmed with XRD. The NFs are evaluated for the CO<sub>2</sub> reduction reaction (CO<sub>2</sub>RR) over various temperatures (25, 30, 35, and 40 °C). The highest Faradaic efficiencies to formate (FE<sub>HCOO-</sub>) are reached by NiO:SnO<sub>2</sub> NFs containing 50% of NiO and 50% SnO<sub>2</sub> (NiOSnO50NF), and 25% of NiO and 75% SnO<sub>2</sub> (NiOSnO75NF), at an electroreduction temperature of 40 °C. At 40 °C, product distribution is assessed with *in-situ* differential electrochemical mass spectrometry (DEMS), identifying methane besides other products, like formate, hydrogen, and carbon monoxide, in the flow electrochemical cell. XPS and EELS unveiled the FE<sub>HCOO-</sub> variations due to a synergistic effect between Ni and Sn. DFT-based calculations reveal the superior thermodynamic stability of Ni-containing SnO<sub>2</sub> systems towards CO<sub>2</sub>RR over the pure oxide systems. Furthermore, computational surface Pourbaix diagrams showed that the presence of Ni as a surface dopant increases the reduction of the SnO<sub>2</sub> surface and enables the production of formate. Our results highlight the synergy between NiO and SnO<sub>2</sub>, which can promote the electroreduction of CO<sub>2</sub> at temperatures above room temperature.



## 1. Introduction

View Article Online  
DOI: 10.1039/D4TA04116J

Anthropogenic CO<sub>2</sub> emissions are a problem that must be addressed to decelerate greenhouse effects like global warming. According to the Intergovernmental Panel on Climate Change (IPCC) published in 2021, the planet's temperature may increase by 1.5 °C in the following decades due to the accelerated release of CO<sub>2</sub> and other greenhouse gases, posing a threat to the global ecosystems and humankind.<sup>1</sup> A call-to-action part of the energy transition goals is CO<sub>2</sub> recycling and utilization. One way to recycle and utilize CO<sub>2</sub> is by producing CO<sub>2</sub>-based value-added products electrochemically. For example, electrochemical CO<sub>2</sub>RR can enable the production of C1 (e.g., CO, HCOO<sup>-</sup>, CH<sub>4</sub>) and C2 (e.g., C<sub>2</sub>H<sub>4</sub>, alcohol) products. The selectivity of C1 or C2 products is often attributed to the catalyst type or the operation conditions during CO<sub>2</sub> electrolysis. As for the catalysts, three different groups of metals have been recognized based on the product generated: formate (e.g., Sn,<sup>2</sup> Pb,<sup>3</sup> Bi,<sup>4,5</sup> In<sup>6</sup>, Hg<sup>7</sup>), CO (Au,<sup>8</sup> Ag,<sup>9</sup> Pd,<sup>10</sup> Zn<sup>11</sup>, Ni<sup>12</sup>), hydrocarbons and alcohols (Cu<sup>13,14</sup>) and other multi-carbon products like amino acids,<sup>15</sup> which in combination with CO<sub>2</sub> and nitrogenated sources (NH<sub>4</sub>HCO<sub>3</sub>) has been demonstrated to lead to the formation of serine.<sup>16,17</sup> Among the mentioned metals, Cu is a catalyst capable of producing C1, C2, and higher multi-carbon products.<sup>18</sup> However, copper exhibits low selectivity, resulting in a mixture of gaseous and liquid reaction compounds. Therefore, the selective production of CO<sub>2</sub>-reduction products is a key challenge that needs attention. One way to overcome this challenge is by synthetically designing a catalyst with earth-abundant elements that can cope with CO<sub>2</sub>RR on an industrial level aimed at 90% conversion to a single product and elevated electrolyzer temperatures for practical reasons (e.g., increased reaction rates or reduced overpotentials).

The reaction temperature is a crucial yet sometimes overlooked parameter in electrochemistry that can compensate for the thermal losses during CO<sub>2</sub> electrolysis. Mizuno et al. have delved into the electrochemical reduction of CO<sub>2</sub> with various electrode compositions.<sup>19</sup> In a different study, Kim et al. analyzed the effect of operating conditions, including temperature, on the electrochemical conversion of CO<sub>2</sub> to formic acid.<sup>20</sup> Like Mizuno et al., the results underscore the intricate relationship between temperature and selectivity for CO<sub>2</sub>RR. Recently, Lowe et al. addressed in depth how temperature variations can influence transport and, thus, formate production.<sup>21</sup> According to the authors, the



temperature notably impacts the reaction selectivity at an industrially accepted current density of 200 mA.cm<sup>-2</sup>. Specifically, the FE<sub>HCOO</sub><sup>-</sup> decreases from 89% at 20 °C to 85% at 70 °C, while the production of CO increases from around 7% to 11%. Interestingly, variations of  $\pm 10\%$  during FE<sub>HCOO</sub><sup>-</sup> have been observed at the assessed temperatures with current densities of up to 1,000 mA.cm<sup>-2</sup>. The results from Lowe et al. indicate that with an increase in temperature, the selectivity towards formate decreases while it increases for other products like CO or H<sub>2</sub>. Other studies reported similar trends, ascribing the decreased formate production and selectivity with increasing temperature to the kinetic effects and CO<sub>2</sub> solubility.<sup>22</sup> Under other conditions, e.g., by varying the electrolyte solution, a fundamental understanding of the relationships between the surface coverage, pH, and kinetics has been proposed for Cu.<sup>18, 23</sup> The previously cited seminal works are therefore used as a stepping stone to understand the temperature effects over NiO:SnO<sub>2</sub> catalyst, whose synergistic combinations can lead to tuning the selectivity of CO<sub>2</sub>RR products. It should be noted that other studies for NiO, SnO<sub>2</sub>, and their combinations do not deal with temperature variation conditions during CO<sub>2</sub> electrolysis (**Tables S1, S2, and S3**). NiO typically leads to CO, CH<sub>4</sub>, and, in some cases, to HCOO<sup>-</sup> (**Table S1**), while SnO<sub>2</sub> leads to HCOO<sup>-</sup> as the main product (**Table S2**). However, their synergistic effect has only been shown HCOO<sup>-</sup> products near room temperature (**Table S3**).

An additional expected challenge for a single oxide composition like SnO<sub>2</sub> is its instability under cathodic electrochemical potentials.<sup>24</sup> The instability of SnO<sub>2</sub> during CO<sub>2</sub>RR can be attributed to the thermodynamic formation of various oxidized tin species.<sup>25</sup> Mu et al. highlighted the dominance of hydroxyl radicals in the reoxidation of oxide-derived metals like Cu. Despite being thermodynamically unstable under cathodic conditions, the authors propose that the presence of Cu<sup>δ+</sup> species enables the CO<sub>2</sub>RR.<sup>26</sup> The results from Mu et al. emphasize the importance of the stability of metal oxide catalysts.<sup>26</sup> Lately, Jiang et al. have discussed the importance of stabilizing the oxidation state of SnO<sub>2</sub> to achieve highly selective CO<sub>2</sub> electroreduction to formate.<sup>27</sup> Their study emphasizes the necessity of maintaining the oxidation state of tin during the CO<sub>2</sub>RR, achieved by incorporating Cu single atoms into the SnO<sub>2</sub> lattice. Like single-atom catalysis, other strategies such as engineering the defects in oxides, has been proposed to tune the selectivity of CO<sub>2</sub>RR<sup>28</sup> and NO<sub>x</sub> reduction reactions.<sup>28,29</sup> From the later examples,



catalyst discovery should favor thermodynamically stable catalytic species that appropriately control product selectivity over various reaction conditions. This could be the case for catalysts that incorporate suitable supports or modifiers optimized for various temperature conditions to minimize the degradation of the active sites.

Aside from single Cu atoms and others like Pt and Bi,<sup>27</sup> NiO is an exciting option to stabilize SnO<sub>2</sub> because it can be incorporated in much higher proportions using electrospinning.<sup>30,31</sup> The incorporation of NiO and SnO<sub>2</sub> goes hand in hand with the possibility of achieving 1D nanofibrous structures to produce non-woven architectures ideal for transport control during electrochemical reactions.<sup>32,33</sup> Herein, our working hypothesis is that NiO embedding will stabilize the SnO<sub>2</sub> and increase the hydrogenation activity of SnO<sub>2</sub>, further enabling the formate (HCOO<sup>-</sup>) production. However, it is not 'a priori' clear how NiO and SnO<sub>2</sub> combined in an NF can synergistically favor formate production and how temperature affects selectivity. Thus, it is essential to explore.

In this work, we employ electrospinning to synthesize different NiOSnO<sub>2</sub> NFs by varying Ni:Sn precursor molar ratios between 75:25, 50:50, and 25:75. Among the applied Ni:Sn molar ratios, 50:50 and 75:25 resulted in an NF-like morphology after annealing at 550 °C while other molar ratios or single compositions did not lead to NFs. Therefore, a detailed structural and morphological characterization (XRD, HR-SEM, and STEM-EDX) is carried out for the 50:50 (NiOSnO50NF) and 25:75 (NiOSnO75NF) NFs. Additionally, XPS and EELS are used to understand the chemical environment before and after the CO<sub>2</sub>RR. The results show the presence of Ni<sup>3+</sup> species and partially reduced SnO<sub>2</sub> after CO<sub>2</sub> electrolysis at 40 °C. The selectivity of the NFs is evaluated by using an electrochemical flow cell with a maximum heating capacity of 40 °C. The electrochemical experiments for NiOSnO50NF and NiOSnO75NF show HCOO<sup>-</sup> selectivities close to □25% at 25 °C, while at temperatures of 30 °C and 35 °C the HCOO<sup>-</sup> selectivity increased to □30% and □50%. An additional increase in selectivity is found at an electroreduction temperature of 40 °C, ca. □85%, and □70% for NiOSnO50NF and NiOSnO75NF, respectively. The product distribution assessed with *in-situ* DEMS aligns with the products observed in the flow cell experiments carried out at 40 °C, where, besides methane (CH<sub>4</sub>), HCOO<sup>-</sup>, hydrogen (H<sub>2</sub>), and carbon monoxide (CO) products have also been found. DFT modeling



provides insights into the reaction mechanism and the effect of temperature during the CO<sub>2</sub>RR process. Furthermore, the computational surface Pourbaix diagram indicates that combining NiO and SnO<sub>2</sub> increases the hydrogenation level in the catalyst model, enabling HCOO<sup>-</sup> production. Our results highlight the importance of catalyst discovery, as demonstrated by the synergistic effects between NiO and SnO<sub>2</sub>, which can boost the electroreduction of CO<sub>2</sub> at temperatures higher than room temperature.

View Article Online  
DOI: 10.1039/D4TA04116J





## 2. Methods

View Article Online  
DOI: 10.1039/D4TA04116J

### 2.1 Synthesis of NiO:SnO<sub>2</sub> nanofibers

The electrospinning technique was used to synthesize metal oxide NFs. For the NiO:SnO<sub>2</sub> NF, NiCl<sub>2</sub>•6H<sub>2</sub>O (ACS grade, Sigma Aldrich) and SnCl<sub>2</sub>•XH<sub>2</sub>O (ACS grade, Sigma Aldrich) were used as precursors. The stock solutions containing Ni, Sn, or their combinations were prepared by dissolving the metal salts in ethanol (100% Tech. grade, BOOM B.V., The Netherlands). Subsequently, polyvinylpyrrolidone (PVP, MW ~1,300,000 by LS, Sigma Aldrich) is added to the solution and stirred magnetically overnight. The precursor solutions were spun using a commercial electrospinning system from IME Technologies (The Netherlands) at 2.0 mL/h. NFs were obtained at 10.25 kV using a stainless-steel needle of 0.4 mm inner diameter. The collector was maintained at a separation distance of 12 cm from the needle to the aluminum collector plate. The NFs were collected at 22 °C and a relative humidity of 30%. After deposition, NFs were dried in a furnace at 80 °C for 12 h to remove the excess solvent. In a subsequent step, the NFs were annealed in two steps in air. First, the NFs were annealed at 350 °C (ramp-up rate of 1 °C/min) for 3 h to remove the organic components. Second, the NFs were annealed at 550 °C (1 °C/min) for 1 h to produce the NiO:SnO<sub>2</sub> mixed oxides. Controls were produced using the electrospinning precursor mentioned above. The controls lead to nanoparticles (NP), hereafter labeled as NiOSnONP. In short, the control samples were prepared by directly pouring the electrospinning precursor into porcelain crucibles and calcined at 550 °C (1 °C/min) for 1 h in air.

### 2.2 Morphological, structural and chemical characterization

#### 2.2.1 HR-SEM

High-resolution (HR)-SEM images were taken using a Zeiss MERLIN SEM microscope operated at 1.4 kV coupled with a High-Efficiency Secondary Electron Detector (HE-SE2). Samples were mounted on conductive carbon tape for analysis with no other preparation.

#### 2.2.2 STEM and EELS

Annular Dark Field (ADF) Scanning transmission electron microscopy (STEM) was performed in a JEOL ARM 200 CF system operated at 80 kV. During imaging, the estimated current density was 14.5 pA while using 68-175 mrad of the annular detector's inner and outer angles. The microscope is equipped



with an SDD Jeol Centurio Energy-Dispersive X-ray (EDX) spectrometer and a GIF Quantum (Gatan) Dual Electron Energy Loss Spectroscopy (EELS) spectrometer. STEM samples were prepared by dispersing 5 mg of NF sample in ethanol and sonicated for 5 min. The suspension was drop cast on Cu grids.

### 2.2.3 X-ray diffraction

X-ray powder diffraction was performed in a Bruker D2 PHASER diffractometer, using Cu K $\alpha$  radiation ( $\lambda = 1.5418 \text{ \AA}$ ) operated at 30V, 10mA, in a range between  $2\theta = 20-85^\circ$ , employing a step size of  $0.05^\circ$  and a scan speed of  $0.1^\circ/\text{s}$ . A low background sample holder (Bruker) was used for the powder samples.

### 2.2.4 Chemical Surface Analysis

X-ray photoelectron spectroscopy (XPS) analysis was performed in a Kratos AXIS ULTRA spectrometer using monochromated Al K $\alpha$  (1486.58 eV). The electron binding energies were referenced to aliphatic carbon C 1s at 284.8 eV. The obtained peak analysis was made using the XPSPEAK41 software. Construction and peak fitting of synthetic peaks in narrow region spectra used a Shirely-type background, and the synthetic peaks were of a mixed Gaussian(30%)-Lorentzian(70%) type.

## 2.3 Electrochemical characterization

### 2.3.1 Electrochemical Flow Cell

The electrochemical cell for CO<sub>2</sub>RR consisted of a custom-made microfluidic flow cell using a filter-press configuration. First, catalyst ink was made to prepare the working electrodes. The catalyst ink consisted of a mixture of 3 mg of multiwalled carbon nanotubes (MWCNTs), 7 mg of catalyst material, 228  $\mu\text{L}$  of 5 wt.% Nafion perfluorinated solution (Nafion and catalyst + MWCNTs in 1:1 ratio by weight) and 600  $\mu\text{L}$  of 2-propanol. Then, MWCNTs are added to the ink to increase the conductivity of the samples. In all samples, the final loading of the catalysts was  $1.25 \text{ mg/cm}^2$ , covering a geometrical area of  $1.8 \text{ cm}^2$  of the cathode. The working electrode consists of carbon gas diffusion electrodes (GDE) (SIGRACET 25BC) sprayed with the catalyst ink and dried at  $80^\circ\text{C}$ . Commercial Ir-MMO and leak-free Ag/AgCl electrodes were used as anode and reference electrodes, respectively. The Nafion 117 membrane separates the cathode and anode chambers. The potential was referred to against the reversible hydrogen electrode (RHE).



$$U^{\text{RHE}} = U(\text{Ag}/\text{AgCl}) + U_0(\text{Tp})\text{A}^{\text{g}/\text{AgCl}} + 0.059\text{pH} \quad (1)$$

View Article Online  
DOI: 10.1039/D4TA04116J

The electroreduction was performed by applying a potential of -0.85 V (vs. RHE) for 2 h, using 0.5 M  $\text{KHCO}_3$  as the electrolyte in both chambers, circulated at 23 mL/min.  $\text{CO}_2$  gas was fed at 11 mL/min. The pH value of the  $\text{CO}_2$ -saturated electrolyte at 40 °C was 7.9. The different temperatures for electroreduction (25, 30, 35, and 40 °C) were controlled by placing the electrolyte reservoirs in a hot water bath and keeping the cell insulated. The maximum temperature capacity of our electrochemical cell was 40 °C.

An online gas chromatograph (Agilent micro-GC) was connected to the electrochemical cell to analyze the gas products ( $\text{H}_2$  and  $\text{CO}$ ). No  $\text{CH}_4$  was observed, possibly due to the low concentration, and thus, below the detection limit of the micro-GC. After electrolysis, liquid products were analyzed with HPLC (AMinex column HPX-87X from Bio-Rad). The eluent used was 5 mM of  $\text{H}_2\text{SO}_4$  with a 0.6 mL/min flow rate at 65 °C. Typically, 10 mL of collected catholyte was mixed with 4 M of  $\text{H}_2\text{SO}_4$  to decrease from pH 7.9 to pH 1-3, corresponding to formic acid formation. It should be noted that all current densities are expressed as cathodic currents. Thus, a negative value was used in the manuscript.

The Faradaic efficiency (FE) for the products was calculated according to the following equation:

$$\text{FE} (\%) = \frac{(\text{Nr})(n)(F)(V)}{Q} \quad (2)$$

where  $\text{Nr}$  is the number of electrons involved in obtaining the product  $r$  ( $2e^-$  for the formate,  $\text{CO}$ , and  $\text{H}_2$ ),  $n$  corresponds to the number of  $r$  moles generated,  $F$  is the Faraday's constant (96,485 C/mol),  $V$  is the molar flow rate of  $\text{CO}_2$  and  $Q$  is the total charge passed during electrolysis.

### 2.3.2 Electrochemical surface area and electrochemical impedance

The electrochemical surface area for the samples was estimated by obtaining the corresponding double-layer capacitance ( $C_{\text{dl}}$ ) from cyclic voltammetry (CV). CV for the working electrodes in the non-faradaic region was recorded in 0.5 M  $\text{KHCO}_3$ , continuously purged with  $\text{N}_2$  at scan rates from 5 mV/s to 80 mV/s. The  $C_{\text{dl}}$  was estimated for all catalysts from the slope of the linear relationship between the current density in the non-faradaic region and the scan rates in the CV. Electrochemical impedance spectroscopy



(EIS) was carried out in the presence of 0.5 M  $\text{KHCO}_3$  as a supporting electrolyte. EIS was done by applying a sinusoidal signal of 10 mV amplitude in the frequency range from  $10^5$  to 0.1 Hz at an employed potential of  $-1.1$  V vs. SHE in the absence of  $\text{CO}_2$  at 25 °C, while in the presence of  $\text{CO}_2$  at 25 and 40 °C.

### 2.3.3 *In-situ* DEMS

An *in-situ* DEMS cell at three electrodes was used to record the ionic current and faradic current versus potential characteristics during cathodic polarization. As for DEMS, the same WE, CE, and RE were employed. The working electrode was prepared on a glassy carbon electrode (3 mm diameter), as described in the previous section. The ionic current (mass signal) for selected mass-to-charge ratios ( $m/z$ ) was recorded simultaneously with the CV profiles at a scan rate of 1 mV/s. The CV measurements were conducted in a  $\text{CO}_2$ -saturated 0.5 M of  $\text{KHCO}_3$  solution within a potential window from 0.45 to  $-1.13$  V (vs. RHE) at 40 °C. The heating increment was made with a heating resistance controlled by an Ink-bird ITC-308-WIFI controller. The ionic current (mass signal) for selected mass-to-charge ratios ( $m/z$ ) was also recorded simultaneously with the faradic current-time profile (I-t). The electrochemical cell was connected to the quadrupole mass spectrometer (Prisma QMG220) at a working pressure of ca.  $2.7 \times 10^{-5}$  mbar.

## 2.4 Theoretical Methods

### 2.4.1 First-principles calculations

Spin-polarized Density Functional Theory (DFT) calculations were employed to investigate the structure and thermodynamic stability of  $\text{SnO}_2(110)$  models (see 2.4.1.1) using the plane wave Vienna Ab initio Simulation Package (VASP).<sup>34,35</sup> The  $\text{SnO}_2(110)$  surface was typically the most abundantly exposed surface, with and without Ni doping, corresponding with  $2\theta = 26.5^\circ$ .

The generalized gradient approximation (GGA) with Perdew-Burke-Ernzerhof (PBE) exchange–correlation functional was employed to compute the total energies.<sup>36</sup> The projector-augmented wave (PAW) pseudopotentials were used for the calculations with an energy cutoff of 400 eV for the plane waves.<sup>37,38</sup> More in particular, 4, 6, 10, and 1 valence electrons were considered for Sn ( $5s^25p^2$ ), O ( $2s^22p^4$ ), Ni ( $3d^84s^2$ ), and H ( $1s^1$ ) atoms, respectively. The Grimme-D3(BJ) method was



implemented in VASP 5.4.4 to account for the van der Waals interactions.<sup>39, 40</sup> The atomic positions were optimized using the conjugate gradient algorithm with force and electronic convergence criteria of 0.01 eV/Å and 10<sup>-5</sup> eV, Gaussian smearing of 0.05 eV, and a 4 × 3 × 1 Monkhorst-Pack k-point grid.<sup>41</sup> The Partial Hessian Vibrational Analysis (PHVA) was carried out only for the surface species and selected atoms at the active sites on the catalyst (involving three Sn and three bridging O atoms) surface while keeping the other atoms fixed (**Figure S1**). The numerical partial Hessian was calculated by displacing the unfixed atoms in x, y, and z-directions with ± 0.01 Å, and the corresponding vibrational modes were obtained by a singular value diagonalization procedure as implemented in the post-processing toolkit TAMKIN.<sup>42</sup> The zero-point corrections and free energy contributions to the reaction energies were determined from the PHVA-based partition functions to determine the pressure and temperature dependence of the Gibbs free energies.

#### 2.4.1.1 Models

The xNi@SnO<sub>2</sub>(110) surface slabs (where x = 0, 1, 2) were constructed with 4 SnO<sub>2</sub> layers, the same number of layers used in previous studies.<sup>43</sup> We opted for the SnO<sub>2</sub>(110) surface since it was known for its thermodynamic stability and has garnered significant interest in experimental and theoretical investigations.<sup>44–48</sup> The periodic slab models considered in the study were referred to as SnO<sub>2</sub>, Ni@SnO<sub>2</sub>, and 2Ni@SnO<sub>2</sub> (**Figure 1**). A vacuum of 15 Å was employed in the z-direction to avoid interactions between periodic images. The Ni@SnO<sub>2</sub> systems were constructed by replacing surface Sn atoms with Ni. To understand the effect of H adsorption on the studied systems during the CO<sub>2</sub> reduction at the cathode, the 2-fold coordinated O atoms (denoted as Sn-O-Sn) on the surface were hydroxylated, forming Sn-(OH)-Sn. A subsequent H addition to Sn-(OH)-Sn results in adsorbed water bonded to two Sn-sites, i.e., Sn-(OH<sub>2</sub>)-Sn. Additionally, larger supercell models were constructed to shed light onto the interface between NiO and SnO<sub>2</sub>. (see section 15 in SI for details).



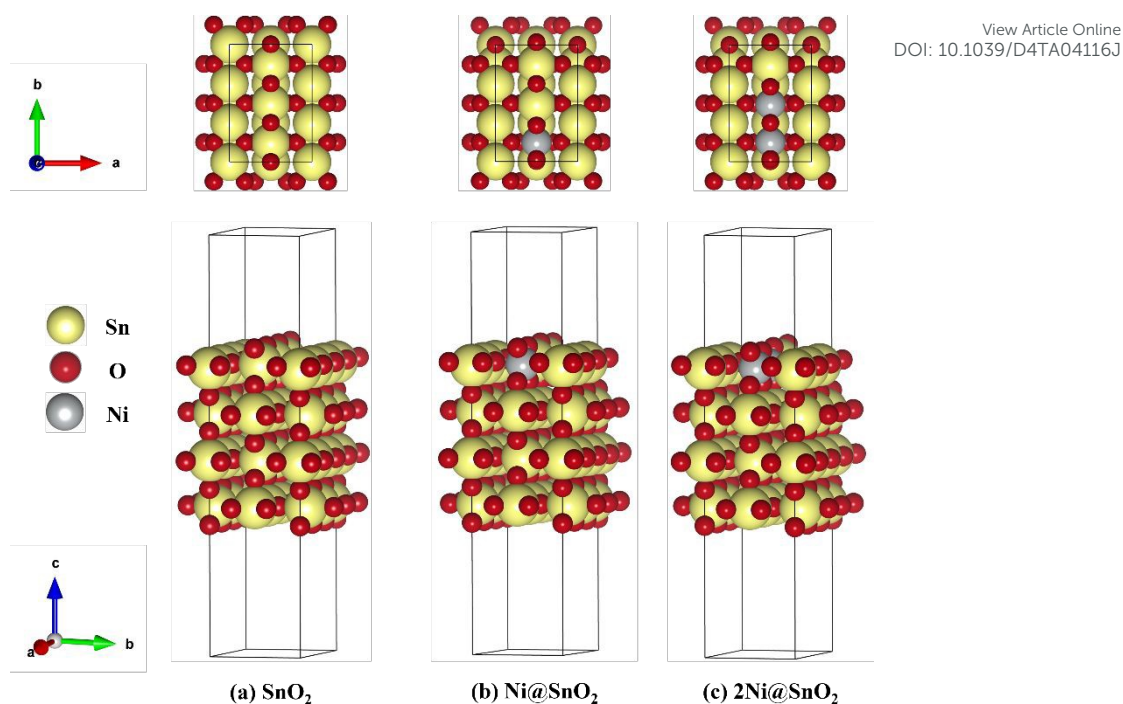
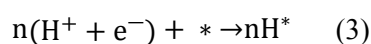


**Figure 1.** Top and side view of chosen SnO<sub>2</sub>(110) model systems for (a) bare SnO<sub>2</sub>, (b) single Ni-doped SnO<sub>2</sub> (Ni@SnO<sub>2</sub>), and (c) double Ni-doped SnO<sub>2</sub> (2Ni@SnO<sub>2</sub>) systems.

### 2.4.2 Surface Pourbaix diagram

Surface Pourbaix diagrams (SPDs) were used to investigate the thermodynamically stable terminations of all studied systems as a function of pH and electrode potential,  $U_{\text{SHE}}$  (Standard Hydrogen Electrode at pH=0,  $P_{\text{H}_2}$  = 1 bar,  $T$  = 26.85 °C, i.e., 300K.<sup>49</sup> Model systems up to a maximum coverage of 2H per bridging O were considered for all studied systems to construct the SPDs.

The adsorption of  $n$  hydrogens on the SnO<sub>2</sub> surfaces can be given by:



where  $*$  represents the SnO<sub>2</sub> (110) surface model onto which the hydrogen atoms can be adsorbed.

The change in Gibbs free energy upon  $n$  hydrogenation reactions with respect to the pristine SnO<sub>2</sub> (110) surface models (**Figure 1**) is given by;

$$\Delta G = G_{n\text{H}^*} - G^* - n\left(\frac{1}{2}G_{\text{H}_2}\right) \quad (4)$$

However, to calculate and construct the Pourbaix diagrams, the change in Gibbs free energy corresponding to a sequential hydrogenation reaction is calculated as a function of electrode potential and pH as follows;



$$\Delta G(\text{pH}, U_{\text{SHE}}) = G_{\text{nH}^*} - G_* - n \left( \frac{1}{2} G_{\text{H}_2}^0 - k_{\text{B}} T \ln(10) \cdot \text{pH} - e \cdot U_{\text{SHE}} \right) \quad (5)$$

View Article Online  
DOI: 10.1039/D4TA04116J

where  $G_{\text{nH}^*}$  and  $G_*$  represent the free energy of the pristine and  $n$  times hydrogen-loaded model systems, respectively. The Gibbs free energy was computed for all terminations, and for a given pH and  $U_{\text{SHE}}$  conditions, the surface termination with the lowest  $\Delta G(\text{pH}, U_{\text{SHE}})$  was considered when constructing the SPD. In the case of two competing terminations, the  $\Delta G(\text{pH}, U_{\text{SHE}})$  term was equated, i.e.,  $\Delta G_A(\text{pH}, U_{\text{SHE}}) = \Delta G_B(\text{pH}, U_{\text{SHE}})$  and the pH vs  $U_{\text{SHE}}$  conditions was isolated to plot the equilibrium lines in the SPD.  $G_{\text{nH}^*}$  can be further described in terms of its vibrational contributions:

$$G_{\text{nH}^*} = E_{\text{DFT}} + E_{\text{ZPVE}} + \Delta E_{\text{vib}}(T) - TS_{\text{vib}} \approx E_{\text{DFT}} + F_{\text{vib}}(T) \quad (6)$$

Here,  $E_{\text{DFT}}$  represents the total energy while  $F_{\text{vib}}$  is the Helmholtz vibrational energy. For the gas phase molecules, the thermodynamic quantities such as ZPE,  $\int_0^{298} C_v dT$ , TS, were obtained from the ideal gas approximations from a previous report. (**Table S4**) The Gibbs free energy for the gas molecules at 25 °C (i.e., 298 K) and 1 atm is given as:

$$G = H - TS = E_{\text{DFT}} + E_{\text{ZPE}} + \int_0^{298} C_v dT - TS + PV \quad (7)$$

where  $E_{\text{DFT}}$ ,  $E_{\text{ZPE}}$ ,  $\int_0^{298} C_v dT$  and  $S$  denote the electronic energy, zero-point vibrational energy, heat capacity, and entropy, respectively.





### 3. Results and discussions

View Article Online  
DOI: 10.1039/D4TA04116J

#### 3.1 Synthesis of NiO:SnO<sub>2</sub> nanofibers

Electrospinning is used to produce NiO:SnO<sub>2</sub> NFs. NFs are synthesized in various compositions, changing the molar ratios between Ni and Sn, i.e., 75%:25% (NiOSnO25NF), 50%:50% (NiOSnO50NF), and 25%:75% (NiOSnO75NF). Similarly, NiO and SnO<sub>2</sub> single compositions have been electrospun. However, NiO and SnO<sub>2</sub> do not lead to NFs under similar electrospinning conditions. The latter includes NiO and SnO<sub>2</sub> formulations, which lose the NF shape after annealing. For instance, a single electrospun composition of NiO and SnO<sub>2</sub> NF can lead to the formation of nanoparticles after annealing (**Figure S2**). Like NiO and SnO<sub>2</sub>, NiOSnO25NF led to nanoparticle formation after annealing (**Figure S3**). The previous results indicate that the spun NFs could not retain the fiber shape during annealing due to the unstable formation of metal oxide, leading to NF-shape coalescence. Similar results have been observed for NiO systems, indicating that our NiCl<sub>2</sub>-PVP formulation leads to nanoparticle (NP) upon annealing.<sup>12</sup> This can also be the case for SnO<sub>2</sub>, which could occupy additional metal oxide agents to maintain the NF shape.<sup>50</sup> Due to the lack of NF shape, NiOSnO25NF has not been analyzed further. However, NiO and SnO<sub>2</sub> are still used as controls, along with NiOSnO50NP and NiOSnO75NP, which both lack NF shape.

NiOSnO50NF and NiOSnO75NF are inspected with STEM-ADF and STEM-EDX, as shown in **Figure 2**. For NiOSnO50NF, **Figure 2a-d** displays an NF-like shape with an NF diameter of 209±45 nm. The NiOSnO50NF comprises ~50 nm nanocrystals and multiple ~10 nm nanocrystals or smaller in diameter. The inner structure corresponds to a polycrystalline arrangement of nanoparticles with some gaps between them. Interestingly, in some cases, a row of nanocrystals forms a string along the NF with higher contrast (e.g., **Figure 2d-e**, yellow arrows). From STEM-EDX mapping Ni, Sn, and O (**Figure 2e'-e'''**), we have identified that these nanoparticle rows primarily comprise oxidized Sn. The contrast over the rows is attributed to densified oxidized Sn. In addition, within the NiOSnO50NF, oxidized Ni has been found to a lesser extent over the NF body; however, larger NiO particles, typically ~200 nm in diameter, decorate the NF morphology. A closer look at the interface between the NiO:SnO<sub>2</sub> nanocrystallites is discussed in **Figure S4**. For NiOSnO75NF in **Figure 2f-i**, the NF is more compact





than in NiOSnO50NF, where nanocrystals are relatively smaller with a 35 nm diameter or less (e.g., **Figure 2i**, yellow arrow). The presence of nanocrystals along the NF shape forming bright strings is less evident than in NiOSnO50NF. Moreover, NiO forms patches over the NF morphology (e.g., **Figure 2j**, yellow arrow). The STEM-EDX mapping for Ni, Sn, and O in **Figure 2j'-j'''** supports these results (see yellow arrows). The presence of Ni within the NF morphology is also verified by the STEM-EDX line scan (**Figure 2i** and **Figure 2k**, see dashed yellow line). The STEM-EDX line scan demonstrates that the Ni remains within the NF body but to a lower extent when compared to Sn (**Figure 2k**). The NiOSnO75NF chemical species have also been investigated with EELS after CO<sub>2</sub> electroreduction (**Figure 2l** and **Figure 2m**). In **Figure 2l**, the EELS signals for NiOSnO75NF after 22 h of CO<sub>2</sub> electroreduction (NiOSnO75NF22h, black line) show that the oxidized tin resembles SnO<sub>2</sub> (blue line). However, we should not disregard the possibility of partially reduced SnO<sub>2</sub> since the NiOSnO75NF22h has some similarities to SnO (red line). It is then suggested that NiOSnO75NF22h contains multiple oxidized Sn species (SnO<sub>x</sub>). In **Figure 2m**, the Ni L23 edge is used to obtain the L3/L2 ratio and determine the chemical environment of Ni-species in NiOSnO75NF after 2 h of CO<sub>2</sub> electroreduction (NiOSnO75NF2h) and NiOSnO75NF22h. The EELS L3/L2 ratio shows that for NiOSnO75NF2h, more points have a wider L3/L2 ratio,<sup>12</sup> indicating a higher fraction of Ni<sup>2+</sup> and Ni<sup>3+</sup> species than NiOSnO75NF22h, which reveals a narrower L3/L2 ratio, close to Ni<sup>3+</sup> species. The results denote that uncoordinated Ni<sup>3+</sup> species, e.g., defects, are formed more due to longer electrolysis time attributed to the loss of NF shape after CO<sub>2</sub> electrolysis.<sup>12</sup>

View Article Online  
DOI: 10.1039/D4TA04116J



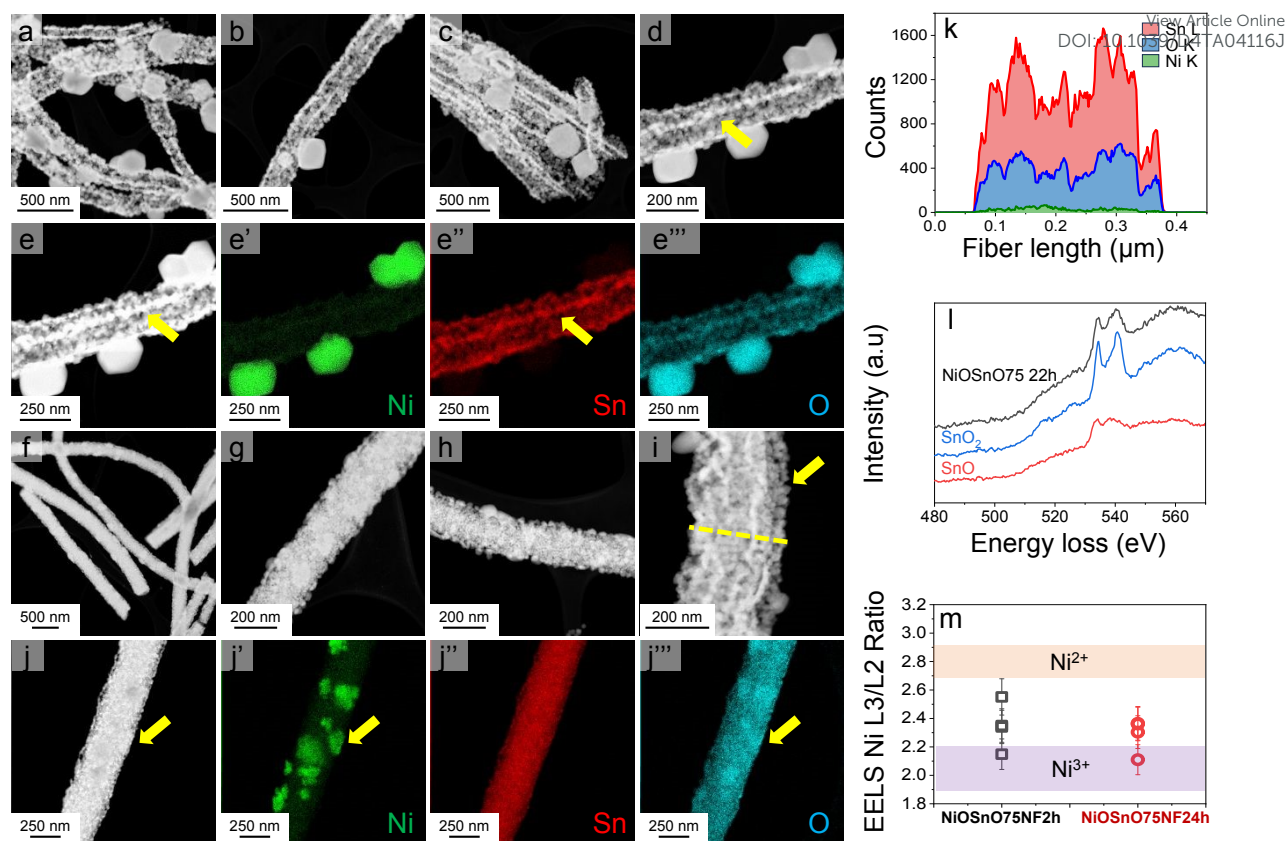


**Figure 2.** STEM-ADF images (Figures 2a-2e) and STEM-EDX maps (Figures 2e'-e''') for NiOSnO50NF. STEM-ADF images (Figures 2f-2j) and STEM-EDX maps (Figures 2j'-j''') for NiOSnO75NF. The STEM-EDX line scan for NiOSnO75NF22h is shown in Figure 2k. EELS measurements NiOSnO75NF22h are shown in Figure 2l-2m for Sn and Ni, respectively. SnO<sub>2</sub> (blue line) and SnO (red line) controls are presented in Figure 2l. In Figure 2m, the L3/L2 ratio of Ni L<sub>23</sub> edge EELS for NiOSnO75NF2h and NiOSnO75NF22h are carried out over different surface areas of the crystallites.

From the STEM-EDX results in Figure 2, we can verify the presence of metal oxides. To confirm the oxide type, we look at the structural characteristics of NiOSnO50NF and NiOSnO75NF using XRD (Figure 3), with NiO and SnO<sub>2</sub> as controls. First, we describe the diffractograms of NiO and SnO<sub>2</sub>. NiO has several diffraction peaks at  $2\theta = 37.2^\circ, 43.3^\circ, 62.9^\circ, 75.4^\circ, \text{ and } 79.3^\circ$ , which correspond to (111), (200), (220), (311), (222) crystallographic planes from NiO (JCPDS 65-6920), respectively.<sup>51</sup> SnO<sub>2</sub> also shows diffraction peaks at  $2\theta = 26.5^\circ, 33.9^\circ, 37.9^\circ, 51.8^\circ, 54.6^\circ, 57.8^\circ, 61.8^\circ, 64.7^\circ, 66.0^\circ, 71.3^\circ, \text{ and } 78.7^\circ$ , corresponding to (110), (101), (200), (211), (220), (002), (310), (112), (301), (220), and (321)



crystallographic planes from SnO<sub>2</sub> respectively (JCPDS No. 41-1445).<sup>52–54</sup> Comparing NiO and SnO<sub>2</sub> with NiOSnO50NF and NiOSnO75NF, we observed that the crystallographic phases correspond to NiO and SnO<sub>2</sub>. No changes in the diffraction peak positions for NiOSnO75NF used as control are observed. No evidence of a difference in crystallographic phase has been found, indicating that NiO and SnO<sub>2</sub> prevail in separate phases within the NF (Figures 2 and 3).

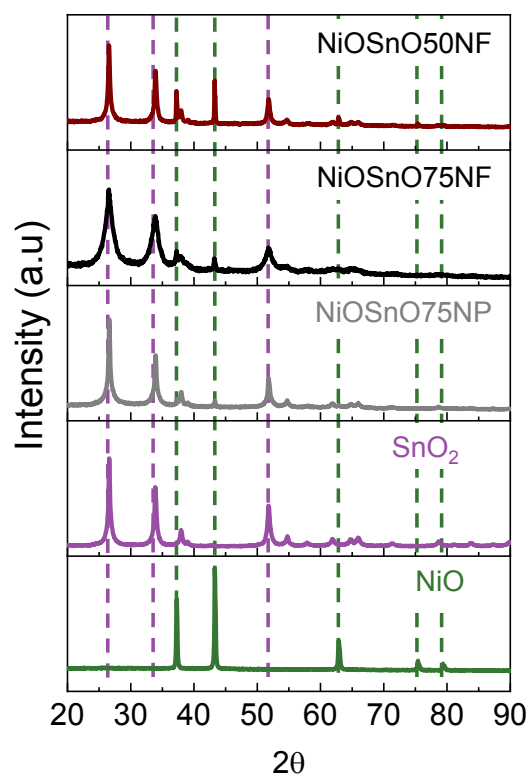


**Figure 3.** XRD diffraction patterns for NiOSnO50NF and NiOSnO75NF. XRD diffraction patterns of NiOSnO75NP, SnO<sub>2</sub>, and NiO are included for controls.

The chemical environment is investigated with XPS to determine the type of species present over NiOSnO50NF and NiOSnO75NF. The XPS core spectra of Ni 2p, Sn 3d, O 1s, and Cl 2p for NiOSnO50NF and NiOSnO75NF are presented in Figure 4. NiO and SnO<sub>2</sub> controls are used for comparison. In Figure 4a, Ni 2p comprises Ni 2p<sub>3/2</sub> and Ni 2p<sub>1/2</sub>. The Ni 2p<sub>3/2</sub> peak can be fitted into two components corresponding to Ni<sup>2+</sup> and Ni<sup>3+</sup> species, labeled in red. Ni<sup>2+</sup> and Ni<sup>3+</sup> peaks are located at 853.8 eV and 855.6 eV.<sup>55–57</sup> The presence of Ni<sup>3+</sup> can be ascribed to the uncoordinated species, like defects.<sup>12</sup> The Ni<sup>3+</sup>/Ni<sup>2+</sup> ratio for NiOSnO50NF is estimated to be close to 2.1, while NiOSnO75NF is around 8.5, indicating that Ni<sup>3+</sup> is more prominent in NiOSnO75NF. Similar Ni<sup>3+</sup>/Ni<sup>2+</sup> has been observed



for NiOSnO50NP and NiOSnO75NP compared to the NF counterpart. Furthermore, a behavior opposite to NiOSnO50NF and NiOSnO75NF has been observed for NiO, in which the Ni<sup>3+</sup>/Ni<sup>2+</sup> ratio is lower, ca. 1.3. Ni<sup>2+</sup> and Ni<sup>3+</sup> species have also been identified with EELS (**Figure 2**), supporting our finding. The results demonstrate that the presence of Sn increases the amount of Ni<sup>3+</sup> species. Next, we analyze the results for Sn 3d. In **Figure 4b**, NiOSnO50NF and NiOSnO75NF show binding energy (BE) for Sn 3d<sub>5/2</sub> around 486.3-486.5 eV, assigned to Sn<sup>4+</sup> in SnO<sub>2</sub>.<sup>58-60</sup> Compared to SnO<sub>2</sub> control with a BE around 486.9 eV associated with Sn<sup>4+</sup>,<sup>61-64</sup> a shift to lower BE has been found for NiOSnO50NF and NiOSnO75NF. This shift can be related to reduced Sn species (e.g., SnO<sub>x</sub>), similar to EELS, as shown in **Figure 2l**.

The XPS core spectra of O 1s and Cl 2p and the fitting curves have also been analyzed (**Figure 4c** and **4d**). O 1s core spectra for NiOSnO50NF and NiOSnO75NF show four different peaks resulting from NiO and SnO<sub>2</sub> formation within the NF body. The O(i) peak (BE 528.8 - 529.1 eV) is attributed to oxygen in NiO.<sup>55,56</sup> The O(ii) peak (BE 530.0 - 530.3 eV) is attributed to mixed oxygen species from NiO and SnO<sub>2</sub>.<sup>57,65,66</sup> The O(iii) peak (BE 531.3 - 531.7 eV) is attributed to surface OH groups.<sup>56,66,67</sup> The O(iv) peak (BE 532.9 - 533.5 eV) is attributed to chemisorbed water.<sup>66,67</sup> Similar results have been obtained for NiO. The O 1s XPS spectrum of NiO shows BE at 529.1 eV, 530.0 eV, 531.5 eV, and 533.3 eV, attributed to oxygen in NiO,<sup>55,56</sup> surface O<sup>2-</sup> species,<sup>68,69</sup> surface OH groups, possibly from uncoordinated Ni<sup>3+</sup> species present in NiO.<sup>12</sup> As for SnO<sub>2</sub>, the O 1s XPS spectrum shows BE at 530.6 eV and 531.8 eV, corresponding to oxygen in SnO<sub>2</sub><sup>70-73</sup> and OH groups.<sup>72,73</sup> Cl 2p core spectra for NiOSnO50NF, NiOSnO75NF, NiO, and SnO<sub>2</sub> show several peaks labeled as Cl(i), Cl(ii), Cl(iii), and Cl(iv). Cl(i) between 198.6-198.1 eV and Cl(ii) between 199.7-200.2 eV are assigned to inorganic chlorine species.<sup>74-77</sup> NiO reveals two additional peaks at Cl(iii) at 200.9 eV and Cl(iv) at 202.5 eV, both corresponding to Cl<sup>-</sup> from different decomposed chemical species of chlorine salt.<sup>12, 78</sup> The concentration of Cl<sup>-</sup> for all the samples remains similar, with an average atomic percentage of 1%±0.2.



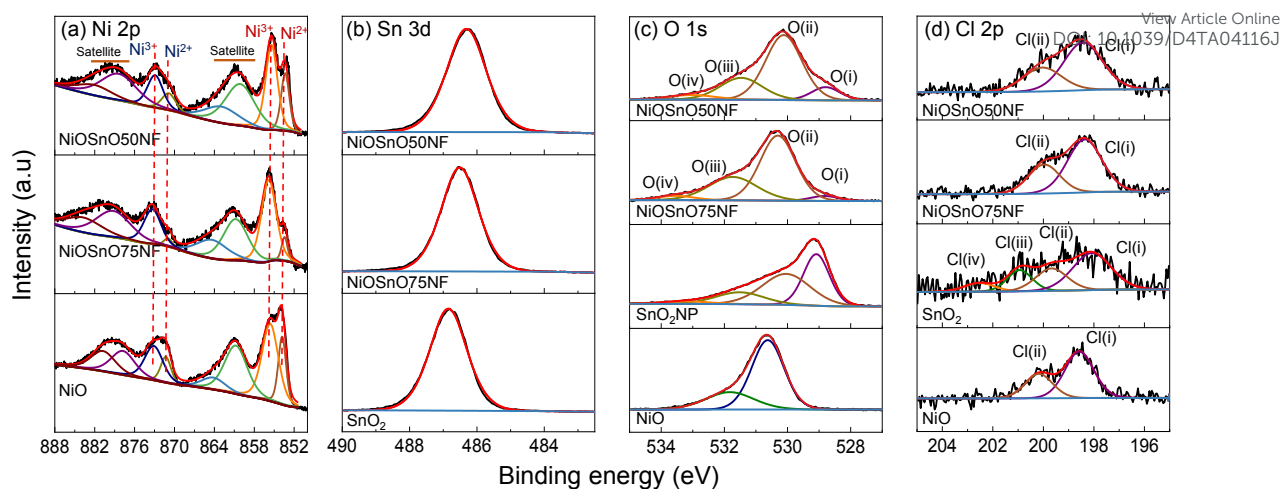


**Figure 4.** (a) Ni 2p, (b) Sn 3d, (c) O 1s, and (d) Cl 2p XPS core spectra for NiOSnO50NF, NiOSnO75NF, NiO, and SnO<sub>2</sub>.

### 3.2 CO<sub>2</sub> electroreduction

The functionality of NiOSnO50NF and NiOSnO75NF is assessed in **Figure 5** for CO<sub>2</sub>RR. To elucidate the effect of NF functionality, NiOSnO50NF and NiOSnO75NF are compared to NiOSnO50NP and NiOSnO75NP, which lack the NF shape. Additionally, the results are contrasted with NiO and SnO<sub>2</sub>. The NiOSnO50NF, NiOSnO75NF, NiOSnO50NP, NiOSnO75NP, NiO, and SnO<sub>2</sub> comparatives are conducted in a flow cell to demonstrate the importance of the synthesized multimetal oxide NFs. Finally, *in-situ* DEMS experiments are discussed to shed light on the product pathways.

The experiments start with preparing the CO<sub>2</sub>RR GDEs by spraying with ink containing MWCNTs, catalyst, and Nafion. The dried GDE is placed in the flow electrochemical cell using a three-electrode configuration containing a solution of 0.5 M KHCO<sub>3</sub> as an electrolyte. The CV in the presence of CO<sub>2</sub> shows the highest current density (J, mA/cm<sup>2</sup>) for the NiOSnO75NF, followed by NiOSnO50NF and SnO<sub>2</sub> with NiO as the lowest J (**Figure 5a**). At 40 °C and -0.85 V vs. RHE, the product distribution for NiOSnO50NP, NiOSnO75NP, NiO, and SnO<sub>2</sub> are also evaluated (**Figure 5b**). It should be noted that three different potentials have been used, i.e., -0.75, -0.85, and -0.95 V vs. RHE, and -0.85 V is selected since it produced the highest FE<sub>HCOO</sub><sup>-</sup> and J<sub>HCOO</sub><sup>-</sup>. Compared to **Figure 5c** and **Figure 5d**, the results highlight the advantage of the synthesized NFs.



In **Figure 5b**, FE for NiOSnO50NP and NiOSnO75NP at 40 °C displays the product distribution, where HCOO<sup>-</sup>, H<sub>2</sub>, and CO are formed during CO<sub>2</sub> electroreduction. The FE for HCOO<sup>-</sup>, H<sub>2</sub>, and CO for NiOSnO50NP are FE<sub>HCOO<sup>-</sup></sub> = 3.8%, FE<sub>H<sub>2</sub></sub> = 80.7% and FE<sub>CO</sub> = 4.7% with partial J values of J<sub>HCOO<sup>-</sup></sub> = -0.7 mA/cm<sup>2</sup>, J<sub>H<sub>2</sub></sub> = -14.7 mA/cm<sup>2</sup> and J<sub>CO</sub> = -0.9 mA/cm<sup>2</sup>. Similar product distribution is observed for NiOSnO75NP with FE<sub>HCOO<sup>-</sup></sub> = 11.2%, FE<sub>H<sub>2</sub></sub> = 58.0%, and FE<sub>CO</sub> = 10.1% have been found with J<sub>HCOO<sup>-</sup></sub> = -1.7 mA/cm<sup>2</sup>, J<sub>H<sub>2</sub></sub> = -8.8 mA/cm<sup>2</sup> and J<sub>CO</sub> = -1.5 mA/cm<sup>2</sup>. For NiO, a prominent generation of H<sub>2</sub> is observed with FE<sub>H<sub>2</sub></sub> = 72.2% and J<sub>H<sub>2</sub></sub> = -2.7 mA/cm<sup>2</sup>. For the same electrocatalyst, FE<sub>HCOO<sup>-</sup></sub> = 6% and J<sub>HCOO<sup>-</sup></sub> = -0.2 mA/cm<sup>2</sup>, no CO has been detected. It could be argued that to increase HCOO<sup>-</sup> formation, NiO should be selectively shaped as octahedra and not as mixed particle shapes (**Figure 2**).<sup>12</sup> SnO<sub>2</sub> FE for HCOO<sup>-</sup>, H<sub>2</sub>, and CO are 37%, 21%, and 19% with J<sub>HCOO<sup>-</sup></sub> = -5.1 mA/cm<sup>2</sup>, J<sub>H<sub>2</sub></sub> = -2.4 mA/cm<sup>2</sup> and J<sub>CO</sub> = -3.1 mA/cm<sup>2</sup>. The results demonstrate that NiO and SnO<sub>2</sub> synergistic effects are important, particularly for NF morphology (**Figure 5c** and **Figure 5d**).

The effect of the temperature (25, 30, 35, and 40 °C) during CO<sub>2</sub>R for NiOSnO50NF and NiOSnO75NF is evaluated in **Figure 5c** and **Figure 5d**. For NiOSnO50NF (**Figure 5c**), the HCOO<sup>-</sup> has a gradual increase in selectivity as the temperature increases, starting from FE<sub>HCOO<sup>-</sup></sub> = 25.2% at 25 °C and reaching a maximum of FE<sub>HCOO<sup>-</sup></sub> = 85.7% at 40 °C. At 40 °C, the highest J<sub>HCOO<sup>-</sup></sub> is observed (-13.8 mA/cm<sup>2</sup>). For FE<sub>H<sub>2</sub></sub>, we observe a gradual decrease in H<sub>2</sub> generation as a function of temperature, starting from FE<sub>H<sub>2</sub></sub> = 55.4% at 25 °C and reaching a minimum of 7% at 40 °C. The J<sub>H<sub>2</sub></sub> value for NiOSnO50NF follows a similar trend, from J<sub>H<sub>2</sub></sub> = -5 mA/cm<sup>2</sup> at 25 °C, reaching a minimum J<sub>H<sub>2</sub></sub> = -1.2 mA/cm<sup>2</sup> at 40 °C. FE<sub>CO</sub> does not drastically decrease with increasing temperature, maintaining J<sub>CO</sub> around -1 mA/cm<sup>2</sup> across the various conditions, with a FE<sub>CO</sub> = 7.2% at 40 °C. Overall, in NiOSnO50NF, FE<sub>HCOO<sup>-</sup></sub> is favored as temperature increases while maintaining FE<sub>CO</sub> constant and suppressing FE<sub>H<sub>2</sub></sub>. NiOSnO50NF and NiOSnO75NF increase the total current densities (J<sub>T</sub>) with temperature.

Next, the electrochemical performance of NiOSnO75NF during CO<sub>2</sub> electroreduction is discussed (**Figure 5d**). For HCOO<sup>-</sup>, a gradual increase in selectivity, with FE<sub>HCOO<sup>-</sup></sub> = 25% at 25 °C and FE<sub>HCOO<sup>-</sup></sub> = 70% at 40 °C, is observed. At 40 °C, the highest J<sub>HCOO<sup>-</sup></sub> is observed with -26.1 mA/cm<sup>2</sup>. The FE<sub>H<sub>2</sub></sub> in NiOSnO75NF also follows a gradual decrease with increasing temperature, with FE<sub>H<sub>2</sub></sub> = 47.4% at 25 °C





and 15.2% at 40 °C. For H<sub>2</sub>, J remains at J<sub>H<sub>2</sub></sub> = -5 mA/cm<sup>2</sup> from 30 °C to 40 °C. Lastly, FE<sub>CO</sub> presents a gradual decrease with 22.6% at 25 °C and 14.5% at 40 °C with J<sub>CO</sub> = -5 mA/cm<sup>2</sup> for temperatures similar to or higher than 30 °C. Although FE<sub>HCOO<sup>-</sup></sub> for NiOSnO75NF remained 15% lower than for NiOSnO50NF at 40 °C, NiOSnO75NF has a 2-fold increase in J<sub>HCOO<sup>-</sup></sub>. This 2-fold increase can be attributed to an increase in the electrochemical surface area (ECSA) as the obtained double-capacitance is higher for NiOSnO75NF (4.68x10<sup>-4</sup> mF/cm<sup>2</sup>) than NiOSnO50NF (3.78x10<sup>-4</sup> mF/cm<sup>2</sup>). Furthermore, the results at 40 °C for NiOSnO75NF are substantiated with EIS. EIS reveals less charge transfer resistance and an increased affinity in the presence of CO<sub>2</sub> for NiOSnO75NF (**Figure S5** and **Table S5**). Likewise, there is no significant effect when looking at the Tafel slopes in the presence of CO<sub>2</sub> (**Figure S6** and **Table S6**). The Tafel slopes are somehow similar. Hence, the results indicate the existence of similar rate-determining steps in the presence of CO<sub>2</sub> for temperatures close to 40 °C. Slight variations in the Tafel slopes are observed for temperatures close to 45 °C, suggesting a different rate-determining step associated with other processes, e.g., H<sub>2</sub> competition. The results of the chronoamperometry from **Figures 5c** and **5d** are shown in **Figure S7**.

In short, a trade-off between selectivity and product yield should be found when assessing catalyst performance. However, NiOSnO50NF and NiOSnO75NF resulted in similar trends, elucidating temperature effects, which could be reasonably associated with favored reaction kinetics at high temperatures.<sup>19,20,21</sup> Such effects have not been observed during CO<sub>2</sub> electroreduction using synergistic catalysts shaped as NFs. Hence, the synergistic effects require an understanding of the reaction product to the fullest. Therefore, an *in-situ* DEMS is assessed to generate insight into the reaction product pathway by detecting the formic acid (HCOOH) mass fragments for NiOSnO75NF, as it yielded the highest HCOO<sup>-</sup> production at 40 °C (**Figure 5d**). Mass spectrometric signals corresponding to H<sub>2</sub> (m/z=2), methane (CH<sub>4</sub>, m/z=16), CO (m/z=28), and HCO<sup>-</sup> (m/z=29) from HCOOH,<sup>79</sup> and CV are recorded simultaneously (**Figure 5e**). It should be noted that mass m/z=29 is selected as it is the most pronounced for HCOOH, and in the absence of CO<sub>2</sub>, no CO<sub>2</sub> reaction products are observed (**Figure S8**). Additionally, to corroborate the detection of HCOOH, formic acid is added to the electrolyte, and the mass signals associated with this organic compound are shown in **Figure S9**. Overall, the distribution



of DEMS products confirmed our flow cell observations in **Figure 5d**, except for  $\text{CH}_4$ , which could be expected to be below the detection limit of our gas chromatograph but captured by DEMS. It should be noted that other factors that might change reaction product selectivity to  $\text{CH}_4$  can be related to the DEMS cell configuration as it can impact pH, generating some gradients.<sup>79</sup>

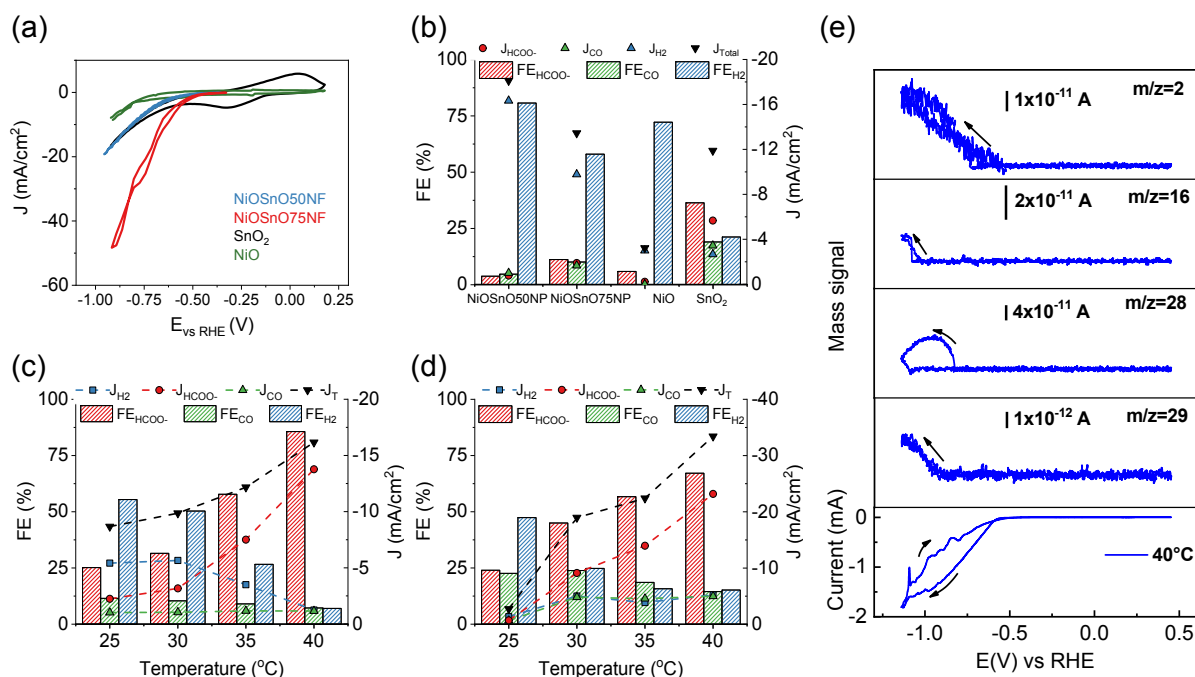


**Figure 5.** (a) CV characteristics of NiOSnO50NF, NiOSnO75NF, NiO, and  $\text{SnO}_2$  at 25 °C. FEs and partial current densities for (b) NiOSnO50NP, NiOSnO75NP, NiO, and  $\text{SnO}_2$  at 40 °C, along with (c) NiOSnO50NF and (d) NiOSnO75NF at -0.85 V vs. RHE for 2 h over various temperatures, i.e., 25, 30, 35, 40 °C. (e) CV characteristic for NiOSnO75NF at 40 °C. In-situ DEMS mass signals recorded at 40 °C are shown as a function of the applied potential (1 mV/s) for  $m/z = 2$ ,  $m/z = 16$ ,  $m/z = 28$ , and  $m/z = 29$ . In all cases, the pH of the bulk electrolyte remained at 7.9.

Lastly, we discuss the effect of uncoordinated Ni species found in NiOSnO NFs, which could have enabled the formation of  $\text{HCOO}^-$ .<sup>12</sup> We could expect NiO species to enhance hydrogenation over  $\text{SnO}_2$ , which is more likely to be as partially reduced  $\text{SnO}_2$ , i.e.,  $\text{SnO}_x$ , after 2 or 22 h  $\text{CO}_2$  electrolysis. Although at 2 h, the NF shape drastically changed its morphology (**Figure S10**), Ni and Sn species remained present even after 22 h of  $\text{CO}_2$  electrolysis (**Figure 2l** and **Figure 2m**). Furthermore, the  $\text{Ni}^{3+}/\text{Ni}^{2+}$  ratios for NFs connect with the improved  $\text{FE}_{\text{HCOO}^-}$  at 40 °C. However, we should not disregard the  $\text{Ni}^{3+}/\text{Ni}^{2+}$





ratio in NPs. For example, the  $\text{Ni}^{3+}/\text{Ni}^{2+}$  ratio for NiOSnO75NP is 7.5, close to NiOSnO75NF (i.e. 8.5).

The benefit of structuring becomes evident when comparing the Raman spectra in **Figure S11** for NiOSnO75NP and NiOSnO75NF. NiOSnO75NP contains more organic species than NiOSnO75NF, compromising the  $\text{CO}_2$  reduction reaction activity (**Figure 2b** and **Figure 2d**).

The results highlight the advantage of the NFs morphology as carbon is removed from the NiOSnO precursor due to the open fibrous structure. Similar effects have been observed for polymer-derived metal oxides, such as 3D-printed structures where carbon remnants are found.<sup>80</sup> Hence, the carbon remnant could act as a blocking layer during  $\text{CO}_2\text{RR}$ , affecting NiOSnO75NP selectivity. This hypothesis is well aligned with NiOSnO75NF loaded with t-octylphenoxypolyethoxyethanol (Triton x100) used as a surfactant, acting as a carbon-blocking agent without compromising the NF morphology after annealing (**Figure S12**). The electrochemical results of NiOSnO75NF loaded with surfactant demonstrate a change in the product distribution with low  $\text{HCOO}^-$  selectivity over the explored temperature ranges (**Figure S13**). The results are substantiated further by ECSA. ECSA result for NiOSnO75NF is  $4.68 \times 10^{-4} \text{ mF/cm}^2$ , while in the presence of a surfactant or NiOSnO75NP, it decreases to  $8.39 \times 10^{-5} \text{ mF/cm}^2$ . Now that we have identified the importance of blocking agent-free catalysts, we propose a mechanism for the NiOSnONF using the most significant products ( $\text{H}_2$  and  $\text{HCOO}^-$ ), as shown in **Figure 5c** and **Figure 5d**.

### 3.3 $\text{CO}_2\text{RR}$ mechanism.

#### 3.3.1 Surface Pourbaix diagrams

Before deriving the  $\text{CO}_2\text{RR}$  mechanism, evaluating the stability of the electrocatalyst and its surface termination at electrochemical conditions is essential. The **supporting information in section 14, Table S7**, describes the stability of the electrocatalyst models in terms of their cohesive and surface formation energy. With an increase in the concentration of Ni in the  $\text{SnO}_2$  surface, the cohesive and surface formation energies become more negative, indicating a favorable formation of Ni-doped  $\text{SnO}_2$  phases. For the pristine NiO, the cohesive energy is more positive (0.161 eV/atom) compared to the Ni-doped  $\text{SnO}_2$  systems (0.061 eV/atom and -0.040 eV/atom, respectively). SPDs have been shown to play a crucial role in elucidating thermodynamically stable terminations as a function of pH and electrode



potential.<sup>12,81,82,83</sup> The calculated SPDs at the experimental electrochemical conditions are shown in [Figure 6](#). View Article Online  
DOI: 10.1039/D4TA04116J

**Figure 6.** The NiO:SnO<sub>2</sub> interface and stability vs potential diagram for all models at pH=0 is displayed in **Figures S14-S17**. In an aqueous environment, the surfaces and active sites tend to hydroxylate (**Figure 6**). **Figures 6a-6c** show the SPDs for the studied SnO<sub>2</sub>(110) model systems with and without Ni doping, which all have 3 bridging oxygens represented by [\*O, \*O, \*O]. In the following, hydrogen coverage refers to these three bridging oxygens, and therefore, 1 ML hydrogen coverage corresponds with the system represented as [\*OH, \*OH, \*OH]. In the potential range of -1.5 to 1.5 V, five different terminations are found in the SPD of the studied pristine SnO<sub>2</sub>(110) surface model (**Figure 6a**). Above 1.21 V and low pH, the configuration with no adsorbed H (or H\*) is stable. As the potential decreases, the adsorption of H gets pronounced, leading to a complete H\* coverage of the bridging O atoms. For instance, between 1.21 V and 0.487 V at pH=0, the termination with 0.33 ML H\* is favored. The other stable terminations are 0.66 and 1.00 ML of H\*. Following the hydration of the oxygens bridging two Sn atoms (Sn-O-Sn), H further absorbs the bridging oxygen, forming water molecules. The termination with 2.00 ML of H [\*H<sub>2</sub>O, \*H<sub>2</sub>O, \*H<sub>2</sub>O] is shown to be favored at potentials lower than -0.69 V. This also implies that the SnO<sub>2</sub> tends to reduce at cathodic electrode potentials, thus forming stable reduced surfaces which can be active for catalysis. The dashed line in red represents the standard OER and HER limits.



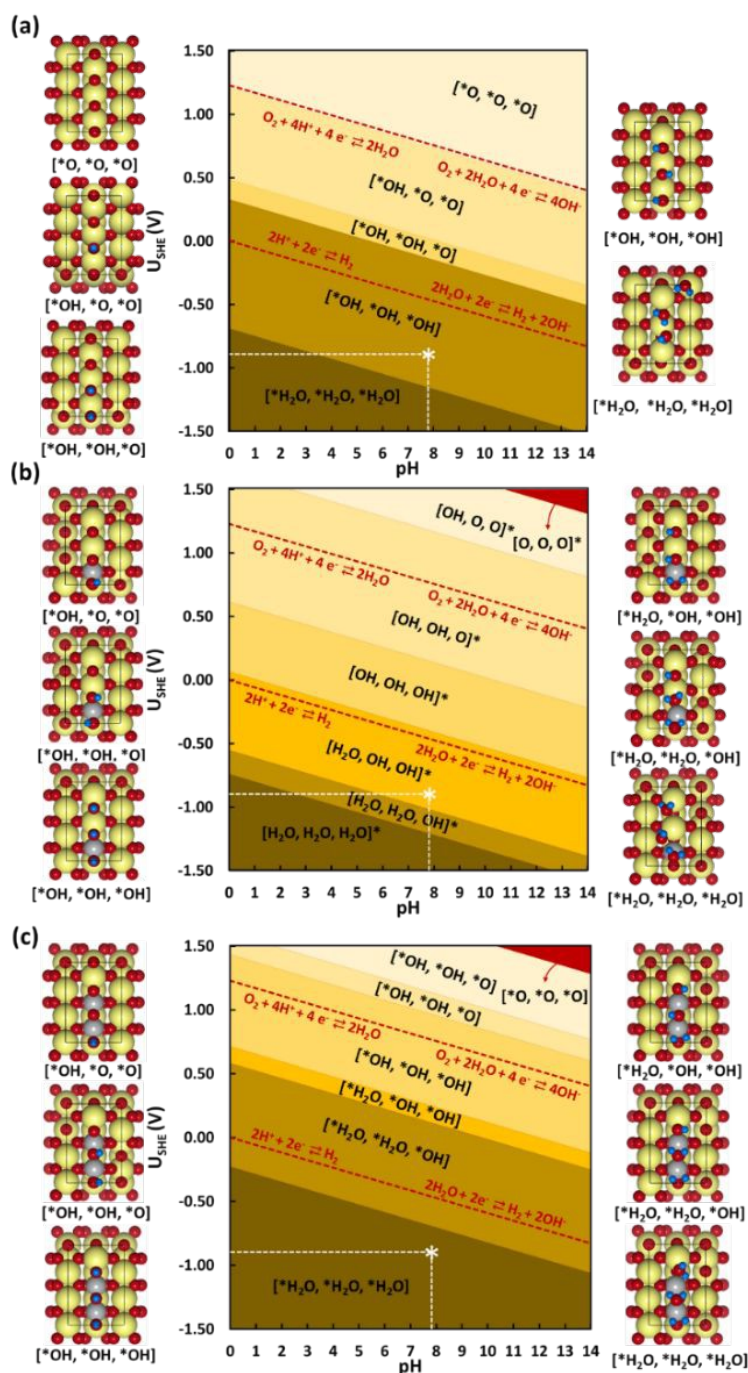


**Figure 6.** Surface Pourbaix Diagrams for the studied (110) surface models (a)  $\text{SnO}_2$ , (b)  $\text{Ni@SnO}_2$ , and (c)  $2\text{Ni@SnO}_2$ . Surfaces with no H adsorbed are colored in red. Color codes: Sn (yellow), O (red), H (blue), and Ni (grey). The white star \* in the diagram corresponds to typical experimental conditions used ( $U_{\text{SHE}} = 0.85 \text{ V}$ ,  $\text{pH} = 7.9$ ).

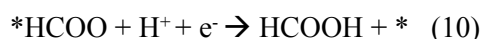
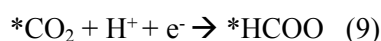
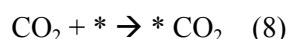
Next, the influence of Ni-doping of the  $\text{SnO}_2(110)$  model system on the Pourbaix diagram is captured in **Figure 6b** and **Figure 6c**. Unlike for  $\text{SnO}_2$ , all H-covered terminations from 0.33 to 2.00 ML  $\text{H}^*$  are



present in the Pourbaix diagram for Ni-doped SnO<sub>2</sub> models at potentials between -1.5 and 1.5 V. In the case of a single Ni-doped SnO<sub>2</sub>(110) system, the surface with no H adsorbed is stable only at higher potentials (>2.14 V) and pH (>13). Between 1.5 and 0.06 V (at pH=0), the two-fold bridging O\* atoms (Sn-O-Sn) tend to get fully hydrogenated. At lower potentials (<0.06 V), the hydrogenated O atoms can adsorb H to form adsorbed water molecules. Below -0.74 V versus RHE, the surface is completely reduced with all two-fold bridging O atoms (Sn-O-Sn) forming water molecules. As a characteristic of H adsorption, on moving to a higher pH (14), the stable H terminations occur at lower potentials with a slope of -59 meV per change in pH of 1. Finally, another Sn atom is replaced with Ni to understand the effect of Ni concentration on the SPDs. For the 2Ni@SnO<sub>2</sub> surface model, all H terminations from 0.33 to 2.00 ML H\* appeared in the Pourbaix diagram. The surface with no hydrogen appears only above 2.10 V and high pH. The termination with 1.00 ML coverage of H is favorable under OER conditions, while the surface with 1.66 ML H\* coverage (2 x H<sub>2</sub>O\*) appears at the HER limit. Interestingly, at the experimental conditions of U=-0.85 V and pH=7.9 (**Figure 5**), the surface with 2.00 ML (3 x H<sub>2</sub>O\*) is likely to be thermodynamically preferred. This also highlights that in CO<sub>2</sub>RR conditions, the surface of the Ni-doped SnO<sub>2</sub> is partially reduced (e.g., SnO<sub>x</sub>, **Figure 2** and **Figure 4**), which could further tailor the electrocatalytic activity at the surface.<sup>84, 85</sup> Overall, the SPDs emphasize the reduction of the SnO<sub>2</sub>-based catalyst surface, specifically the co-adsorption of water molecules at potentials of experimental interest.

### 3.3.2 CO<sub>2</sub>RR Mechanism

The SPDs allow us to determine the relevant active site model termination under operating conditions, and subsequently, CO<sub>2</sub> reduction pathways are determined. A typical reduction of CO<sub>2</sub> to HCOO<sup>-</sup> (i.e., hereafter HCOOH) over SnO<sub>2</sub> occurs via a 2e<sup>-</sup> pathway with the elementary steps described as:



where \* denotes the active site of the catalyst. Although the proton-coupled electron transfer (PCET) mechanism assuming steps with  $H^+/e^-$  pairs (equivalent to  $\frac{1}{2}H_2$ ) is vastly employed in the context of DFT-based studies,<sup>43,48</sup> it usually oversimplifies the catalytic surface in which protons can be supplied from the dissociation of water molecules at the electrode-electrolyte interface. T. Burdyny and W. Smith demonstrated that at current densities above  $35 \text{ mA/cm}^2$ , the proton for  $CO_2$  reduction is supplied by the water molecules on the electrode surface, increasing the local interfacial pH.<sup>86</sup> The resulting change in the local environment further influences the binding energies of intermediates and surface coverage on the electrode. The SPDs discussed previously highlighted this, during which the bridged oxygen forms water molecules at lower potentials with an overall reduction in the catalytic surface. **Figure 7** presents a plausible mechanism for the  $CO_2RR$  to  $HCOO^-$  for the  $SnO_2$ -based models involving a PCET reaction considered in the study. It can be found that the active catalyst surface of  $2Ni@SnO_2$  is covered with 2.00 ML of H (i.e., three  $H_2O$  per unit cell), which is represented as [ $*H_2O$ ,  $*H_2O$ ,  $*H_2O$ ] following its SPD. This model could approximate the local environment on the reduced surface more appropriately than the usual models that do not consider electrolyte species' co-adsorption. Although the three water molecules do not appear in the SPDs of  $SnO_2$  and  $Ni@SnO_2$  at the experimental conditions of  $-0.85 \text{ V}$  and a pH of 7.9, we consider its 2.00 ML coverage models for comparing it with the  $2Ni@SnO_2$  system (**Figure 8**).

Article Online  
DOI: 10.1039/D4TA04116J



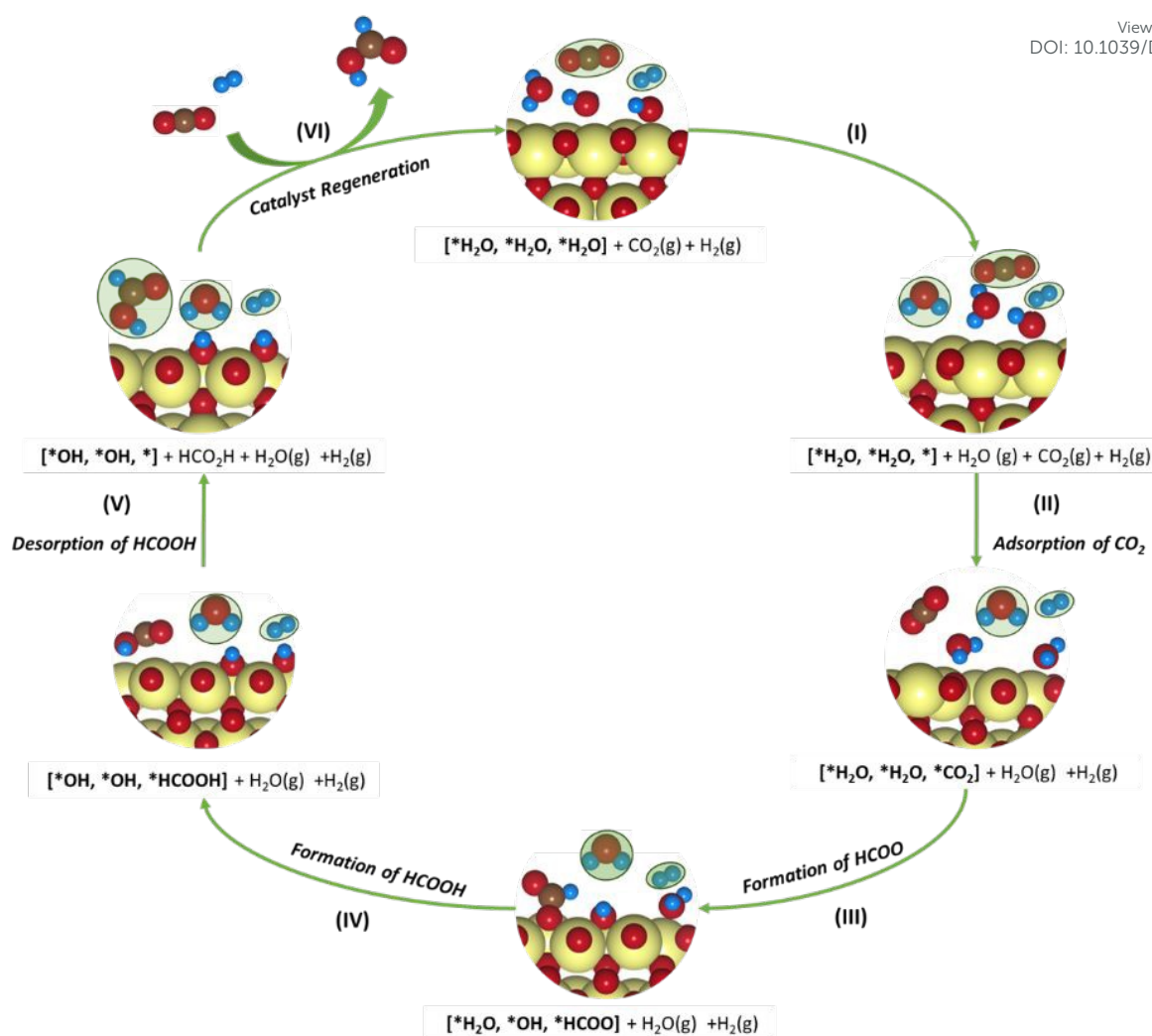


**Figure 7.** Schematic representation of the plausible CO<sub>2</sub> reduction mechanism for the SnO<sub>2</sub>-based model systems. The adsorbates in gaseous states are marked in green.

To understand the thermodynamics feasibility of the reaction pathway proposed, we calculated the Gibbs free energy profile for each model system. The mechanism starts with the desorption of one of the H<sub>2</sub>O molecules on 2Ni@SnO<sub>2</sub>, leaving an empty site for CO<sub>2</sub> adsorption [ $\text{*H}_2\text{O}, \text{*H}_2\text{O}, \text{*}$ ] (**Figure 8**). From **Figure 8**, the process of water desorption is exothermic and exergonic for the Ni-doped SnO<sub>2</sub> (110) systems compared to pure SnO<sub>2</sub>. However, the subsequent CO<sub>2</sub> adsorption on the empty site is endergonic (**Figure 8**), with positive reaction-free energies for SnO<sub>2</sub> (0.524 eV), Ni@SnO<sub>2</sub> (0.152 eV), and 2Ni@SnO<sub>2</sub> (0.194 eV) model systems which becomes more feasible if SnO<sub>2</sub> is Ni doped. Further, upon abstracting an H from a co-adsorbed water molecule,  $\text{*CO}_2$  can form  $\text{*HCOO}$ . For Ni@SnO<sub>2</sub>, the  $\text{*HCOO}$  intermediate is thermodynamically more stable (-1.374 eV, **Figure 8**) compared to pure SnO<sub>2</sub>





(-0.594 eV, **Figure 8**). Interestingly, for 2Ni@SnO<sub>2</sub>, the CO<sub>2</sub> molecule directly tends to form a stable HCOOH, surpassing the \*HCOO intermediate state. The formation of \*HCOOH from \*HCOO and neighboring \*OH<sub>2</sub>, is exergonic for SnO<sub>2</sub> with a reaction-free energy of -1.021 eV, whereas for the Ni@SnO<sub>2</sub> system, this process is endergonic (+0.391 eV) energy. For 2Ni@SnO<sub>2</sub> the \*HCOO intermediate is found to be protonated directly and form \*HCOOH, an overall exergonic process with a reaction-free energy of -0.207 eV. From \*HCOOH, the desorption of HCOOH is endergonic and requires 0.300 eV, 0.478 eV, and 0.610 eV for SnO<sub>2</sub>, Ni@SnO<sub>2</sub>, and 2Ni@SnO<sub>2</sub>, respectively (**Figure 8**). Therefore, it is clear that under certain reaction conditions, the desorption of HCOOH can become the rate-limiting step in the reaction. Especially, for the 2Ni@SnO<sub>2</sub> system, with the highest adsorption free energy barrier for \*HCOOH desorption, temperature facilitates the desorption process given the decreasing free energy differences from 25 °C to 40 °C (**Figure 9**). These findings agree with the temperature-dependent faradaic efficiencies and partial current densities of CO<sub>2</sub> electroreduction (**Figure 5c** and **Figure 5d**). Finally, after the production of HCOOH, the catalyst needs to regenerate to continue with the catalytic cycle. The catalyst regeneration with two H<sup>+</sup>/e<sup>-</sup> pairs is endergonic with the DG increasing in the order: 2Ni@SnO<sub>2</sub> (0.097 eV) < Ni@SnO<sub>2</sub> (1.092 eV) < SnO<sub>2</sub> (1.308 eV), however, this regeneration can happen electrochemically, and under cathodic potentials of -0.90 V vs. RHE this regeneration process will be spontaneous. The regeneration process is more favorable for the surfaces with more Ni species (e.g., Ni<sup>2+</sup> and Ni<sup>3+</sup>), which indicates the influence of Ni doping on the catalytic activity of SnO<sub>2</sub>.

Article Online  
DOI: 10.1039/D4TA04116J



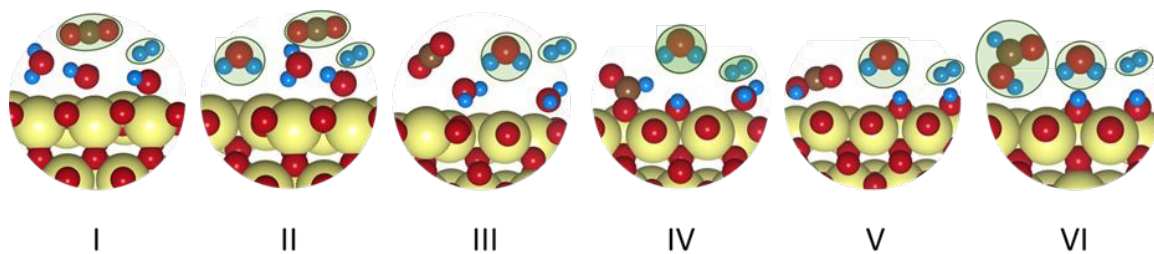
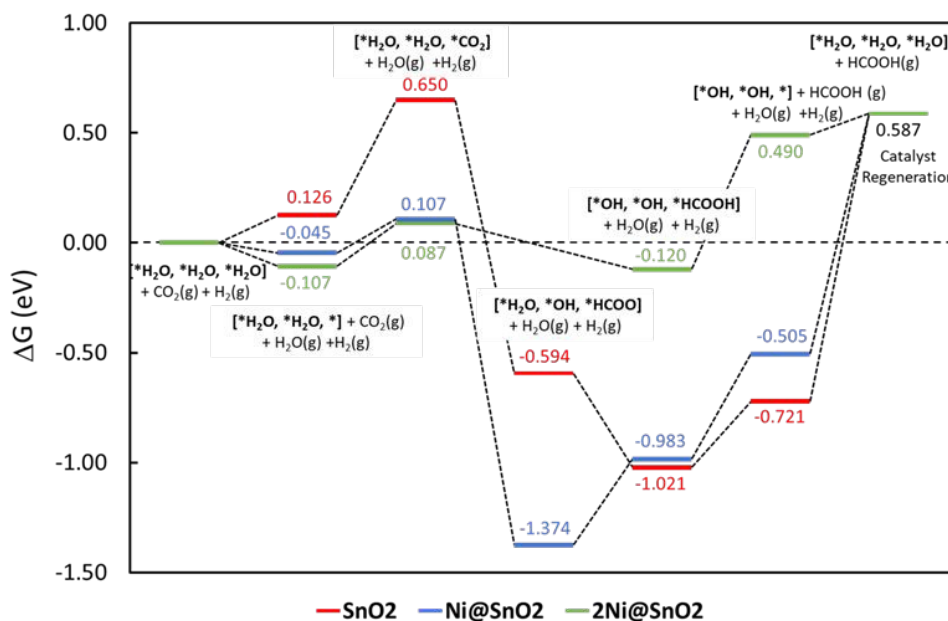


**Figure 8.** Free energy diagram for CO<sub>2</sub> reduction to HCOOH over SnO<sub>2</sub>(110), Ni@SnO<sub>2</sub>(110), and 2Ni@SnO<sub>2</sub>(110) electrocatalyst models. (Bottom panel) The binding modes of the adsorbates on the catalyst at different reaction states and the adsorbates in the gaseous state are marked in green.





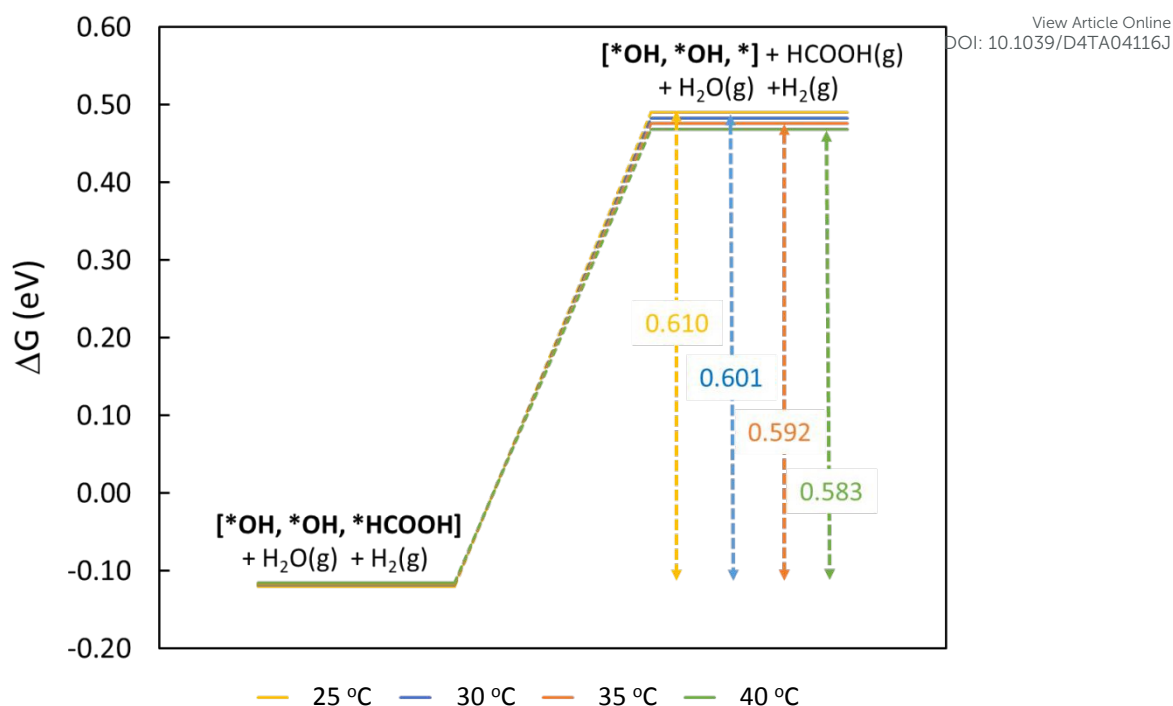


**Figure 9.** Free energy diagram for rate-limiting step of HCOOH desorption as a function of temperature on the 2Ni@SnO<sub>2</sub>(110) model.

#### 4. Conclusions

NiOSnO NFs have been synthesized by electrospinning. NiOSnONFs effectively function as electrocatalysts for the electrochemical CO<sub>2</sub>RR, yielding HCOO<sup>-</sup> beyond the room temperature suitable to current electrolyzers. The highest Faradaic efficiencies to formate are achieved with NiOSnO50NF and NiOSnO75NF at an electroreduction temperature of 40 °C. XPS and EELS analyses reveal a synergistic effect between the Ni and Sn species. Electrochemical measurements and *in-situ* DEMS provide insights into product distribution during CO<sub>2</sub>RR. Computational Pourbaix diagrams show that this synergistic effect arises from the dissolution of NiO under reducing conditions. DFT calculations show that embedding Ni in SnO<sub>2</sub> is energetically more favorable in addition to aiding the reduction of the SnO<sub>2</sub> surface under relevant electroreduction conditions. The desorption of HCOOH is the rate-limiting step whose free energy decreases with increasing temperature from 25 °C to 40 °C, which agrees with the temperature-dependent faradaic efficiencies and partial current densities found during the experiments. Looking into the future, it is clear that catalysts like NiOSnO NFs can be further designed for other temperature conditions rather than room temperature and will, in the future, be used in CO<sub>2</sub>



electrolyzer technologies over various temperature ranges. These findings underscore the significance of catalyst discovery and explore the potential for temperature-driven synergistic effects in metal oxide catalysts for CO<sub>2</sub> electroreduction.

View Article Online  
DOI: 10.1039/D4TA04116J



## Author contributions

View Article Online  
DOI: 10.1039/D4TA04116J

M.A.R.O., R.L., M.V., and A.S.A. designed the experiments, analyzed the data, and wrote the first draft of the manuscript. M.A.R.O., M.S., C.F., and E.C.-M. synthesized the material and carried out electrochemical measurements. R.L. and M.V performed the DFT calculations (1) to construct the computational Pourbaix diagrams, and (2) to unravel the relevant CO<sub>2</sub> reduction pathways. F.R.-Z. performed STEM-related analysis. The initial idea was coined by A.M., C.F., T.K., J.G.E., M.V., and A.S.A. All authors contributed to the final draft.

## Competing interests

The authors declare no competing interests.

## Acknowledgments

The authors thank Mark Smithers and Gerard Kip (MESA+ Institute, University of Twente) for their support. The research leading to this report's results has received funding from the European Research Council (ERC) under the European Union's Horizon 2020 research and innovation program (Grant Agreement No. 742004). R.L. (GOIPG/2022/442) thanks the Irish Research Council (IRC) for an IRC postgraduate fellowship. R.L. and M.V. acknowledge the Irish Centre for High-End Computing (ICHEC) for the computational facilities and support. M.S. and T.K. acknowledge funding from the Jane and Aatos Erkkö foundation (USVA project). In addition, F.R.-Z. Acknowledges the European Research Council (ERC) Starting Grant 123STABLE (Grant agreement ID: 852208).



## References

- 1 V. Masson-Delmotte, P. Zhai, A. Pirani, S. L. Connors, C. Péan, S. Berger, N. Caud, Y. Chen, L. Goldfarb, M. I. Gomis, M. Huang, K. Leitzell, E. Lonnoy, J. B. R. Matthews, T. K. Maycock, T. Waterfield, O. Yelekçi, R. Yu and B. Zhou, *IPCC, 2021: Climate Change 2021: The Physical Science Basis. Contribution of Working Group I to the Sixth Assessment Report of the Intergovernmental Panel on Climate Change*, Cambridge University Press, 2021
- 2 X. Bai, W. Chen, C. Zhao, S. Li, Y. Song, R. Ge, W. Wei and Y. Sun, *Angewandte Chemie*, 2017, **129**, 12387–12391.
- 3 F. Köleli and D. Balun, *Appl Catal A Gen*, 2004, **274**, 237–242.
- 4 K. Fan, Y. Jia, Y. Ji, P. Kuang, B. Zhu, X. Liu and J. Yu, *ACS Catal*, 2020, **10**, 358–364.
- 5 B.-Q. Miao, W.-S. Fang, B. Sun, F.-M. Li, X.-C. Wang, B.-Y. Xia and Y. Chen, *Chinese J Struct Chem*, 2023, **42**, 100095.
- 6 R. Hegner, L. F. M. Rosa and F. Harnisch, *Appl Catal B*, 2018, **238**, 546–556.
- 7 W. Yang, S. Chen, W. Ren, Y. Zhao, X. Chen, C. Jia, J. Liu and C. Zhao, *J Mater Chem A*, 2019, **7**, 15907–15912.
- 8 W. Zhu, R. Michalsky, Ö. Metin, H. Lv, S. Guo, C. J. Wright, X. Sun, A. A. Peterson and S. Sun, *J Am Chem Soc*, 2013, **135**, 16833–16836.
- 9 S. Liu, H. Tao, L. Zeng, Q. Liu, Z. Xu, Q. Liu and J. L. Luo, *J Am Chem Soc*, 2017, **139**, 2160–2163.
- 10 D. Gao, H. Zhou, J. Wang, S. Miao, F. Yang, G. Wang, J. Wang and X. Bao, *J Am Chem Soc*, 2015, **137**, 4288–4291.
- 11 J. Rosen, G. S. Hutchings, Q. Lu, R. V. Forest, A. Moore and F. Jiao, *ACS Catal*, 2015, **5**, 4586–4591.
- 12 M. A. Rodriguez-Olguin, C. Flox, R. Ponce-Pérez, R. Lipin, F. Ruiz-Zepeda, J. P. Winczewski, T. Kallio, M. Vandichel, J. Guerrero-Sánchez, J. G. E. Gardeniers, N. Takeuchi and A. Susarrey-Arce, *Appl Mater Today*, 2022, **28**, 101528.
- 13 A. Vasileff, C. Xu, Y. Jiao, Y. Zheng and S. Z. Qiao, *Chem*, 2018, **4**, 1809–1831.
- 14 S. Nitopi, E. Bertheussen, S. B. Scott, X. Liu, A. K. Engstfeld, S. Horch, B. Seger, I. E. L. Stephens, K. Chan, C. Hahn, J. K. Nørskov, T. F. Jaramillo and I. Chorkendorff, *Chem Rev*, 2019, **119**, 7610–7672.
- 15 C. Englezos, A. Raman, D. Jonker, N. A. Ramos-Delgado, M. Altomare, H. Gardeniers and A. Susarrey, *Chempluschem*, 2024, **89**, e202300763.
- 16 Y. Fang, X. Liu, Z. Liu, L. Han, J. Ai, G. Zhao, O. Terasaki, C. Cui, J. Yang, C. Liu, Z. Zhou, L. Chen and S. Che, *Chem*, 2023, **9**, 460–471.
- 17 Y. Fang, L. Han and S. Che, *Chinese J Struct Chem*, 2023, **42**, 100107.
- 18 R. E. Vos, K. E. Kolmeijer, T. S. Jacobs, W. Van Der Stam, B. M. Weckhuysen and M. T. M. Koper, *ACS Catal*, 2023, **13**, 8080–8091.
- 19 T. Mizuno, K. Ohta, A. Sasaki, T. Akai, M. Hirano and A. Kawabe, *Energy Sources*, 1995, **17**, 503–508.



- 20 H. Y. Kim, I. Choi, S. H. Ahn, S. J. Hwang, S. J. Yoo, J. Han, J. Kim, H. Park, J. H. Jang and S. K. Kim, in *Int J Hydrogen Energy*, Pergamon, 2014, vol. 39, pp. 16506–16512. Article Online  
DOI: 10.1039/D4TA04116J
- 21 A. Löwe, C. Rieg, T. Hierlemann, N. Salas, D. Kopljar, N. Wagner and E. Klemm, *ChemElectroChem*, 2019, **6**, 4497–4506.
- 22 S. T. Ahn, S. Sen and G. T. R. Palmore, *Nanoscale*, 2022, **14**, 13132–13140.
- 23 R. E. Vos and M. T. M. Koper, *ChemElectroChem*, 2022, **9**, e202200239.
- 24 K. Bejtka, J. Zeng, A. Sacco, M. Castellino, S. Hernández, M. A. Farkhondehfar, U. Savino, S. Ansaloni, C. F. Pirri and A. Chiodoni, *ACS Appl Energy Mater*, 2019, **2**, 3081–3091.
- 25 M. He, B. Xu and Q. Lu, *Chinese J Catal*, 2022, **43**, 1473–1477.
- 26 S. Mu, H. Lu, Q. Wu, L. Li, R. Zhao, C. Long and C. Cui, *Nat Commun*, 2022, **13**, 1–8.
- 27 Y. Jiang, J. Shan, P. Wang, L. Huang, Y. Zheng and S. Z. Qiao, *ACS Catal*, 2023, **13**, 3101–3108.
- 28 T. S. Bui, E. C. Lovell, R. Daiyan and R. Amal, *Adv Materials*, 2023, **35**, 2205814.
- 29 E. Castañeda-Morales, J. O. Peralta-Cruz, F. Ruiz-Zepeda, A. Susarrey-Arce, M. L. Hernández-Pichardo and A. Manzo-Robledo, *Mater Today Energy*, 2024, **41**, 101525.
- 30 M. A. Rodríguez-Olguin, R. N. Cruz-Herbert, H. Atia, M. Bosco, E. L. Fornero, R. Eckelt, D. A. De Haro Del Río, A. Aguirre, J. G. E. Gardeniers and A. Susarrey-Arce, *Catal Sci Technol*, 2022, **12**, 4243–4254.
- 31 M. A. Rodríguez-Olguin, H. Atia, M. Bosco, A. Aguirre, R. Eckelt, E. D. Asuquo, M. Vandichel, J. G. E. Gardeniers and A. Susarrey-Arce, *J Catal*, 2022, **405**, 520–533.
- 32 W. Ju, F. Jiang, H. Ma, Z. Pan, Y. B. Zhao, F. Pagani, D. Rentsch, J. Wang and C. Battaglia, *Adv Energy Mater*, 2019, **9**, 1901514.
- 33 X. Zong, Y. Jin, C. Liu, Y. Yao, J. Zhang, W. Luo, A. Züttel and Y. Xiong, *Electrochem commun*, 2021, **124**, 106968.
- 34 G. Kresse and J. Furthmüller, *Comput Mater Sci*, 1996, **6**, 15–50.
- 35 G. Kresse and J. Hafner, *Phys Rev B*, 1994, **49**, 14251–14269.
- 36 J. P. Perdew, K. Burke and M. Ernzerhof, *Phys Rev Lett*, 1996, **77**, 3865–3868.
- 37 D. Joubert, *Phys Rev B Condens Matter Mater Phys*, 1999, **59**, 1758–1775.
- 38 P. E. Blöchl, *Phys Rev B*, 1994, **50**, 17953–17979.
- 39 D. G. A. Smith, L. A. Burns, K. Patkowski and C. D. Sherrill, *J Phys Chem Lett*, 2016, **7**, 2197–2203.
- 40 S. Grimme, S. Ehrlich and L. Goerigk, *J Comput Chem*, 2011, **32**, 1456–1465.
- 41 H. J. Monkhorst and J. D. Pack, *Phys Rev B*, 1976, **13**, 5188–5192.
- 42 A. Ghysels, T. Verstraelen, K. Hemelsoet, M. Waroquier and V. Van Speybroeck, *J Chem Inf Model*, 2010, **50**, 1736–1750.
- 43 S. Ning, J. Wang, D. Xiang, S. Huang, W. Chen, S. Chen and X. Kang, *J Catal*, 2021, **399**, 67–74.



- 44 D. Koziej, K. Thomas, N. Barsan, F. Thibault-Starzyk and U. Weimar, *Catal Today*, 2007, **126**, 211–218. View Article Online  
DOI: 10.1039/D4TA04116J
- 45 I. Manassidis, J. Goniakowski, L. N. Kantorovich and M. J. Gillan, *Surf Sci*, 1995, **339**, 258–271.
- 46 J. Oviedo and M. J. Gillan, *Surf Sci*, 2000, **463**, 93–101.
- 47 L. Braglia, M. Fracchia, P. Ghigna, A. Minguzzi, D. Meroni, R. Edla, M. Vandichel, E. Ahlberg, G. Cerrato and P. Torelli, *J Phys Chem C*, 2020, **124**, 14202–14212.
- 48 C. Salvini, M. Re Fiorentin, F. Risplendi, F. Raffone and G. Cicero, *J Phys Chem C*, 2022, **2022**, 126–14441.
- 49 H. A. Hansen, J. Rossmeisl and J. K. Nørskov, *Phys Chem Chem Phys*, 2008, **10**, 3722–3730.
- 50 M. Safari, J. Mazloom, K. Boustani and A. Monemdjou, *Sci Rep*, 2022, **12**, 1–15.
- 51 Y. Luo, M. Weng, J. Zheng, Q. Zhang, B. Xu, S. Song, Y. Shen, Y. Lin, F. Pan and C. Nan, *J Alloys Compd*, 2018, **750**, 17–22.
- 52 X. Ye, W. Zhang, Q. Liu, S. Wang, Y. Yang and H. Wei, *New J Chem*, 2015, **39**, 130–135.
- 53 P. P. Dorneanu, A. Airinei, M. Grigoras, N. Fifere, L. Sacarescu, N. Lupu and L. Stoleriu, *J Alloys Compd*, 2016, **668**, 65–72.
- 54 N. Van Hieu, P. Thi Hong Van, L. Tien Nhan, N. Van Duy and N. Duc Hoa, *Appl Phys Lett*, 2012, **101**, 1–5.
- 55 A. Kotta, E.-B. Kim, S. Ameen, H.-S. Shin and H. K. Seo, *J Electrochem Soc*, 2020, **167**, 167517.
- 56 X. Xu, L. Li, J. Huang, H. Jin, X. Fang, W. Liu, N. Zhang, H. Wang and X. Wang, *ACS Catal*, 2018, **8**, 8033–8045.
- 57 X. Xu, H. Zhang, Y. Tong, Y. Sun, X. Fang, J. Xu and X. Wang, *Appl Surf Sci*, 2021, **550**, 149316.
- 58 H. Liu, F. Wang, K. Hu, B. Zhang, L. He and Q. Zhou, *Nanomaterials*, 2019, **9**, 1250.
- 59 M. Taño, D. Maestre, J. Ramírez-Castellanos, S. Li, P. S. Lee and A. Cremades, *Nanomaterials*, 2021, **11**, 1–13.
- 60 Q. Ma, H. Li, J. Guo, S. Chu, Q. Zhang and Z. Lin, *Mater Sci Semicond Process*, 2021, **128**, 105762.
- 61 M. Kwoka, L. Ottaviano, M. Passacantando, S. Santucci, G. Czempik and J. Szuber, *Thin Solid Films*, 2005, **490**, 36–42.
- 62 J. Jeong and B. J. Lee, *J Nanosci Nanotechnol*, 2013, **13**, 711–713.
- 63 R. Zhang, Z. Xu, T. Zhou, T. Fei, R. Wang and T. Zhang, *J Colloid Interface Sci*, 2019, **557**, 673–682.
- 64 P. G. Choi, N. Izu, N. Shirahata and Y. Masuda, *Sens Actuators B Chem*, 2019, **296**, 126655.
- 65 M. Kandasamy, A. Seetharaman, D. Sivasubramanian, A. Nithya, K. Jothivenkatachalam, N. Maheswari, M. Gopalan, S. Dillibabu and A. Eftekhari, *ACS Appl Nano Mater*, 2018, **1**, 5823–5836.



- 66 C. N. R. Rao, V. Vijaykrishnan, G. U. Kulkarni and M. K. Rajumon, *Appl Surf Sci*, 1995, **84**, 285–289. Review Article Online  
DOI: 10.1039/D4TA04116J
- 67 Z. Chen, T. Dedova, I. O. Acik, M. Danilson and M. Krunks, *Appl Surf Sci*, 2021, **548**, 149118.
- 68 N. Weidler, J. Schuch, F. Knaus, P. Stenner, S. Hoch, A. Maljusch, R. Schäfer, B. Kaiser and W. Jaegermann, *J Phys Chem C*, 2017, **121**, 6455–6463.
- 69 B. Payne, M. Biesinger, and N. McIntyre, *J. Electron Spectros Relat Phenomena*, 2012, **185**, 159-166.
- 70 J. Jeong and B. J. Lee, *J Nanosci Nanotechnol*, 2013, **13**, 711–713.
- 71 M. Kwoka, L. Ottaviano, M. Passacantando, S. Santucci, G. Czempik and J. Szuber, *Thin Solid Films*, 2005, **490**, 36–42.
- 72 R. Zhang, Z. Xu, T. Zhou, T. Fei, R. Wang and T. Zhang, *J Colloid Interface Sci*, 2019, **557**, 673–682.
- 73 P. G. Choi, N. Izu, N. Shirahata and Y. Masuda, *Sens Actuators B Chem*, 2019, **296**, 126655.
- 74 M. C. Biesinger, L. W. M. Lau, A. R. Gerson and R. S. C. Smart, *Phys Chem Chem Phys*, 2012, **14**, 2434–2442.
- 75 G. E. Wagner, C. D., Briggs, W. M., Davis, L. E., Moulder, J. F. and Muilenberg, in *Handbook of X-ray Photoelectron Spectroscopy*, Perkin Elmer Corp, Physical Electronics Division, 1992.
- 76 C. A. Tolman, W. M. Riggs, W. J. Linn, C. M. King and R. C. Wendt, *Inorg Chem*, 1973, **12**, 2770–2778.
- 77 R. Félix, N. Llobera-Vila, C. Hartmann, C. Klimm, M. Hartig, R. G. Wilks and M. Bär, *RSC Adv*, 2018, **8**, 67–73.
- 78 Y. C. Lin, Y. Y. Chen, B. Y. Yu, W. C. Lin, C. H. Kuo and J. J. Shyue, *Analyst*, 2009, **134**, 945–951.
- 79 J. M. Mora-Hernandez, W. I. González-Suárez, A. Manzo-Robledo and M. Luna-Trujillo, *J CO2 Util*, 2021, **47**, 101504.
- 80 J. P. Winczewski, S. Zeiler, S. Gabel, A. Susarrey-Arce, J. G. E. Gardeniers and B. Merle, *Mater Des*, 2023, **232**, 112142.
- 81 A. Ngoipala, R. Lipin, R. L. Arevalo and M. Vandichel, *Int J Hydrogen Energy*, 2024, **53**, 829–839.
- 82 R. Lipin, A. Ngoipala, R. L. Arevalo and M. Vandichel, *Int J Hydrogen Energy*, 2024, **61**, 460–472.
- 83 J. W. Liao, X. Lu, B. Y. Huang, G. Q. Yu and X. B. Li, *Int J Hydrogen Energy*, 2021, **46**, 9077–9086.
- 84 B. Kumar, V. Atla, J. P. Brian, S. Kumari, T. Q. Nguyen, M. Sunkara and J. M. Spurgeon, *Angewandte Chemie*, 2017, **56**, 3645–3649.
- 85 H. Hu, L. Gui, W. Zhou, J. Sun, J. Xu, Q. Wang, B. He and L. Zhao, *Electrochim Acta*, 2018, **285**, 70–77.
- 86 T. Burdyny and W. A. Smith, *Energy Environ Sci*, 2019, **12**, 1442–1453.



## Data availability statements

View Article Online  
DOI: 10.1039/D4TA04116J

Data are available upon request from the authors

